JGR Oceans

RESEARCH ARTICLE
10.1029/2021JC017762

Key Points:

- Ocean heat transport into the Arctic does not systematically increase with horizontal resolution in the GFDL CM2-O model suite
- The eddy-permitting and eddy-rich configurations show a stronger response to climate change than the eddy-parameterized configuration
- Flow partitioning in the northern North Atlantic and location of deep convection centers are key to the heat transport into the Arctic

Correspondence to:
M. Decuypère,
marine.decuypere@mail.mcgill.ca

Citation:
Decuypère, M., Tremblay, L. B., & Dufour, C. O. (2022). Impact of ocean heat transport on Arctic sea ice variability in the GFDL CM2-O model suite. *Journal of Geophysical Research: Oceans*, *127*, e2021JC017762. https://doi.org/10.1029/2021JC017762

Received 15 JUL 2021
Accepted 14 FEB 2022

Impact of Ocean Heat Transport on Arctic Sea Ice Variability in the GFDL CM2-O Model Suite

Marine Decuypère[1], L. Bruno Tremblay[1], and Carolina O. Dufour[1]

[1]Department of Atmospheric and Oceanic Sciences, McGill University, Montréal, QC, Canada

Abstract The impact of horizontal resolution on meridional Ocean Heat Transport (OHT) and sea ice in the Arctic is investigated using the GFDL CM2-O climate model suite (1°, 1/4°, and 1/10°) in both preindustrial control and climate change simulations. Results show an increase in OHT associated to a decrease in sea ice extent (SIE) in the Arctic on interannual and decadal timescales. This link, however, is not monotonic with spatial resolution. While OHT increases and SIE decreases from the Low to the Medium resolution, the reverse is true from the Medium to the High resolution. Differences in OHT and SIE between the three model configurations mostly arise from the preindustrial state. As the spatial resolution increases, the Irminger Current is favored at the expense of the North Atlantic Drift. This rerouting of water to the Western side of Greenland results in less heat delivered to the Arctic in the High-resolution configuration than in its Medium counterpart. As a result, the Medium-resolution configuration is in best agreement with observed SIE and Atlantic OHT. Concurrent with the change in the partitioning in volume is a change in deep convection centers from the Greenland-Irminger-Norwegian Seas in the Low resolution to the Labrador Sea in the Medium and High resolutions. Results suggest a coupling between OHT into the Arctic and deep convection in the North Atlantic.

Plain Language Summary The Arctic has experienced a dramatic decrease in its sea ice cover over the past four decades. One of the main drivers of this intense melting is ocean heat transport from lower latitudes into the Arctic. This transport takes place at three main gates linking the North Pacific and Atlantic oceans to the Arctic. Thus, proper representation of ocean currents and the associated heat transport is necessary to make accurate projections of the Arctic pack ice in climate models. Here, we study the response of the Arctic sea ice to an increase in atmospheric carbon dioxide concentration using three configurations of a climate model that differ in their horizontal resolution of the ocean. Changing resolution can affect the strength, pattern, and amount of heat carried by the currents. Our results confirm that the greater the ocean heat transport into the Arctic, the lower the sea ice extent. In contrast with previous studies, however, the ocean heat transport does not systematically increase when refining the ocean horizontal resolution. This result points to the fact that not only the currents strength, but also the pathways are influenced by the ocean horizontal resolution, impacting the penetration of warm Atlantic waters into the Arctic.

1. Introduction

Three different ways of improving climate projections are increasing the complexity of climate processes, refining spatial resolution or advancing parameterizations. Refining spatial resolution is costly numerically, as the total integration time increases by a factor of at least 8 for each doubling of horizontal spatial resolution (Flato, 2011). It is also costly in terms of workforce since most parameterizations are still required and must be recalibrated as a function of newly resolved spatial scales (Molinari & Dudek, 1992). Human and computational resources in the last decade have been invested in the development of new or improved parameterizations of subgrid scale processes (e.g., Brankart, 2013; Fox-Kemper et al., 2011; Jansen et al., 2015), increased ensemble size and number of scenarios, as well as on increasing spatial resolution of all the components of the climate system. Still, the majority of the Earth System Models participating to the Coupled Model Intercomparison Project version 6 (CMIP6) DECK use a 1° ocean component that require to employ eddy parameterizations (Hewitt et al., 2020). In the context of Arctic climate, the new parameterizations include surface melt pond (Holland et al., 2012), ice thickness distribution (Bitz et al., 2001; Ungermann et al., 2017), lateral melt (Smith et al., 2021; Tsamados et al., 2015), and ice-ocean heat exchange (Shi et al., 2020), among others. These developments have led to significant improvements in the simulation of the mean state and variability (forced and natural) of the ice-ocean system, including the sea ice thickness distribution (Bitz et al., 2002; Bitz & Roe, 2004; Shi et al., 2020), and

sensitivity of the sea ice cover to increased carbon dioxide (CO_2) concentration (Auclair & Tremblay, 2018; Holland et al., 2006; Jahn et al., 2016; Stroeve et al., 2014).

Recently, climate groups have started to explore the sensitivity of the climate system to an eddying ocean. For instance, the High-Resolution Model Intercomparaison Project (HighResMIP) proposed a common protocol for low (1°) and high (1/4° to 1/12°) resolution model simulations under the umbrella of the World Climate Research Program (WCRP; Haarsma et al., 2016). Studies using global climate models and ocean-only models have investigated the effect of refining spatial resolution on the subpolar gyre and Atlantic water pathways in the northern North Atlantic, Irminger Sea, Labrador Sea, and Baffin Bay in the context of ice shelf-ocean interactions and increased rate of advance of tidewater glaciers (Myers et al., 2007; Straneo & Heimbach, 2013). Marzocchi et al. (2015) find that a high-resolution model (1/12° resolution) leads to an improved representation of the subpolar gyre and a better representation of Labrador Sea Water formation and variability compared to the 1° and 1/4° versions of the same model. Koenigk et al. (2021) find that increasing the ocean model resolution from 1° to 1/4° leads to an increase in deep mixing in the Labrador Sea and draw a direct link between the subpolar gyre strength, surface ocean salinity and depth of convection. García-Quintana et al. (2019) find less formation of Labrador Sea Water in a 1/12° model compared to a 1/4° model, due to a shallowing of the mixed layer and a smaller area of deep convection. Pennelly and Myers (2020) study the impact of resolution (from 1/4° to 1/12° to 1/60°) on Labrador Sea circulation, and find that the mixed layer depth in the Labrador sea is shallower as the resolution increases thanks to an increase in eddy kinetic energy, and that Labrador Sea Waters density is better represented in the 1/60° model.

Several studies showed that an increase in resolution leads to an increase in midlatitude meridional ocean heat transport (OHT) in general (Griffies et al., 2015; Hewitt et al., 2016) and in the Atlantic Ocean in particular (Grist et al., 2018). A better representation of OHT is needed to improve projections of sea ice extent (SIE), as the ocean is one of the main drivers of sea ice loss and variability in the Arctic (Bitz et al., 2005). Indeed, in recent years, an increase in the Barents Sea Opening OHT led Atlantic Waters to penetrate deeper into the Eurasian Basin (Smedsrud et al., 2010), a process known as the Atlantification of the Arctic (Årthun et al., 2012; Polyakov et al., 2017). This was accompanied by a weakening of the stratification in the Eurasian Basin and enhanced vertical heat fluxes from Atlantic Waters (Polyakov et al., 2017), and a limited winter sea ice growth in the Barents Sea (Barton et al., 2018). Variability in Atlantic OHT is responsible for the interannual variability SIE in the Barents Sea (Årthun et al., 2012, 2019). The impact of the Atlantic multidecadal variability on the Arctic SIE has been highlighted especially for Barents Sea ocean surface temperature and ice extent (Årthun et al., 2019; Drinkwater et al., 2014; Mette et al., 2021) and the Greenland Ice Sheet (Drinkwater et al., 2014). Pacific Waters also play a key role in sea ice loss: for instance, Woodgate et al. (2010) argued that a doubling of ocean heat flux through the Bering Strait between 2001 and 2007 was responsible for a third of the 2007 seasonal sea ice loss. Finally, correlation between OHT and SIE is shown at interannual and decadal time scales during rapid decline events in the Community Earth System Model—LE (Auclair & Tremblay, 2018; Li et al., 2017).

While the impact of spatial resolution on global scale circulation patterns has been widely discussed, relatively fewer studies focus on the impact of resolution on OHT and SIE variability in the Arctic Ocean. Griffies et al. (2015) find a lower poleward OHT in the coarse resolution model configuration (1° resolution) than in the finer resolution model configurations (1/4° and 1/10° resolution), due to weaker subtropical and subpolar gyre transports. Furthermore, increased ocean and atmosphere resolutions in the HadGEM3-GC2 model (from 1/4° and 60 km to 1/12° and 25 km, respectively), together with higher coupling frequency lead to stronger boundary currents, increased OHT, warmer surface ocean in the North Atlantic, and lower SIE (Hewitt et al., 2016; Roberts et al., 2016). Similarly, the ocean processes in the ECMWF-IFS are very sensitive to changes in ocean resolution from 1° to 1/4°, especially North Atlantic and Arctic Ocean, with improved representations of the Atlantic Meridional Overtuning Circulation (AMOC), OHT, and sea ice cover (Roberts et al., 2018). A recent study by Docquier et al. (2019) shows that, in the CMIP6 models participating in HighResMIP, the increase of spatial resolution from 1° to 1/4° yields a larger Atlantic OHT and lower sea ice extent and volume. Furthermore, while the models exhibit strong correlations between the Atlantic OHT and the SIE variability in the Barents, Kara, and Greenland Seas, the correlations do not increase uniformly with resolution across the models studied.

In the early 2010s, both the Geophysical Fluid Dynamics Laboratory (GFDL) and the National Center for Atmospheric Research (NCAR) have developed a climate model with an ocean component at 1/10° for century scale simulations of the past, present, and future climate (Delworth et al., 2012; Kirtman et al., 2012). Using the GFDL

1/10° model, Griffies et al. (2015) find that mesoscale eddies play a significant role in the upward vertical heat transport and ocean heat uptake, and that this model yields a generally more accurate representation of global ocean temperature and heat budget. Using the same model, Saba et al. (2016) show that a refined resolution provides a more realistic representation of the Northwest Atlantic Shelf circulation, and a higher warming rate to increased CO_2 forcing. Dufour et al. (2017) show that this same model enables the formation of polynyas in the Weddell Sea compared to a coarser resolution, thanks to a stronger stratification in the Southern ocean and a better representation of transient eddies and topographical features. Drake et al. (2018) find that this fine resolution model leads to a significantly shorter advective upwelling time scale of Circumpolar Deep Waters in the Southern Ocean compared to the coarser resolution configurations, because of eddy variability, thus highlighting the role of mesoscale eddies in large-scale circulation time scale.

In this paper, we use the GFDL CM2-O model suite which comprises three configurations of different horizontal resolutions of the ocean component. We investigate the impact of refining the horizontal grid spacing of the ocean component on OHT in the Arctic, SIE and their relationship. We find that the magnitude of OHT and sea ice are strongly correlated on (multi) decadal time scales; however, the links between OHT and SIE at interannual scale differ between model configurations. While the increase from the 1° resolution to the 1/4° resolution does lead to an increase in OHT and decrease in SIE, the increase from the 1/4° resolution to the 1/10° leads to an opposite response. In addition, the change in resolution impacts the partitioning of North Atlantic heat transport thus resulting in different sea ice conditions.

The paper is structured as follows. In Section 2, we present the GFDL CM2-O model suite and the simulations, and we describe the methods used to analyze the model output. In Section 3, we present the SIE and OHT mean states, their response to an idealized climate change simulation as well as the impact of OHT on SIE. In Section 4, we discuss the differences in the ocean circulation in the North Atlantic across the model suite and their potential impact on the OHT and sea ice.

2. Model Description and Simulations

2.1. The CM2-O Model Suite

In this study, we use the GFDL CM2-O model suite which comprises three configurations of the same climate model differing by the horizontal resolution of the ocean component: CM2-1deg (1°; eddy-parameterized), CM2.5 (1/4°; eddy-permitting), and CM2.6 (1/10°; eddy-rich; Delworth et al., 2012; Griffies et al., 2015). In the following, we refer to the three configurations as Low, Medium, and High, respectively.

The ocean component is the version five of the Modular Ocean Model (MOM5; Griffies et al., 2015) run with volume-conserving Boussinesq kinematics. The model uses a tripolar grid, with one pole at the South Pole, and two poles placed over northern Canada and Russia (Figure 1; Murray, 1996). The ocean model is run with a z^* geopotential vertical coordinate (meaning that grid cell thickness is time dependent) and 50 layers in the vertical. At rest, the thickness of the layers ranges from 10 m in the first 250–210 m at the bottom. The thickness of bottom cells is adjusted to match topography using the partial cell method (Pacanowski & Gnanadesikan, 1998). The model uses the piecewise parabolic method for the advection scheme (Delworth et al., 2012), and the nonlocal K-profile parameterization for vertical mixing (Large et al., 1994). The Low-resolution model configuration includes the Ferrari et al. (2010) modified version of the Gent and McWilliams mesoscale eddy parameterization (Gent et al., 1995) with a maximum diffusivity of 1,200 $m^2\ s^{-1}$ (Griffies et al., 2015) compared with 800 $m^2\ s^{-1}$ in the ESM2M Earth System Model (Dunne et al., 2012), a model similar to the Low resolution in many aspects. The Medium-resolution and High-resolution model configurations enable some explicit representation of the mesoscale, though incomplete, and do not use a mesoscale eddy parameterization (Griffies et al., 2015). The resolution needed to resolve the baroclinic deformation radius in the Arctic ranges from 1/12° in the Central Arctic to 1/50° in the shallow waters near the coast (see Figure 2 of Hallberg, 2013). All three model configurations use the submesoscale mixed layer eddy parameterization of Fox-Kemper et al. (2011). Key characteristics of the model configurations are summarized in Table 1.

In the High-resolution configuration, the refined horizontal resolution allows for a better representation of the Gulf of Ob in the Kara Sea and of the Canadian Arctic Archipelago. Key differences between the High resolution and the Medium and Low resolutions also include the resolution of the Alpha and Lomonosov ridges, the Barents Sea and the steepness of the continental slopes. In the Medium resolution, the Victoria Strait, the Coronation

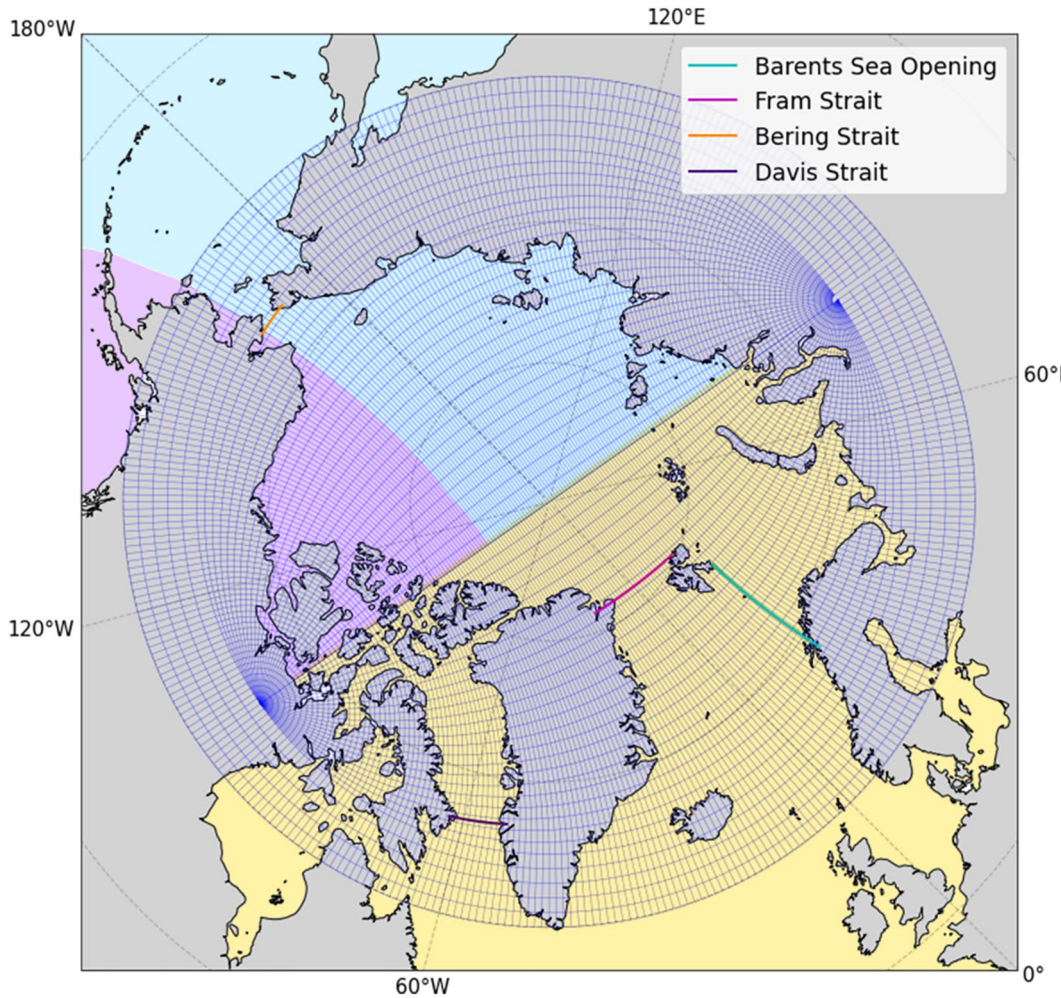

Figure 1. Arctic model domain and tripolar grid in CM2-1deg (Low-resolution model configuration). The main gates used in the study are: the Fram Strait (pink), the Barents Sea Opening (cyan), the Bering Strait (orange), and the Davis Strait (purple). The coastlines are drawn from observations. The three sectors are: the Atlantic sector (yellow), the Pacific sector (purple), and the Eurasian sector (blue).

Gulf, the Prince Regent Inlet, and the Foxe Basin are closed. In the Low resolution, the Fury and Hecla Strait connecting the Gulf of Boothia and Foxe Basin is closed. In contrast, all these basins and straits are open in the High-resolution configuration.

The sea ice component is the GFDL Sea Ice Simulator (SIS) which uses a three-layer Semtner thermodynamic model (one layer of snow, two layers of ice) with five ice thickness categories (Delworth et al., 2006; Semtner, 1976; Winton, 2000) and a brine pocket parameterization (Bitz & Lipscomb, 1999). The model uses the same tripolar grid as the ocean component (Dunne et al., 2012). The dynamic component of the sea ice model uses the elastic-viscous-plastic rheology of Hunke and Dukowicz (1997). The maximum value for albedos is set to 0.85 for snow on ice and 0.68 for bare sea ice (Delworth et al., 2012).

The atmospheric component is the GFDL AM2.1 (Atmospheric Model 2.1). AM2.1 is run on a "cubed-sphere" grid with a horizontal resolution of 50 km and 32 vertical levels (Delworth et al., 2012), compared with 200 km and 24 levels in the GFDL CM2.1 described in Delworth et al. (2006). The advective terms are calculated with a modified Euler backward scheme (Kurihara & Tripoli, 1976). The atmospheric physics module is the GFDL AM2-LM2 model (Anderson et al., 2004) that includes three prognostic tracers for clouds: cloud liquid, cloud ice and cloud fraction. Finally, the suite uses the land component LM3 (Land Model 3) with a drainage route

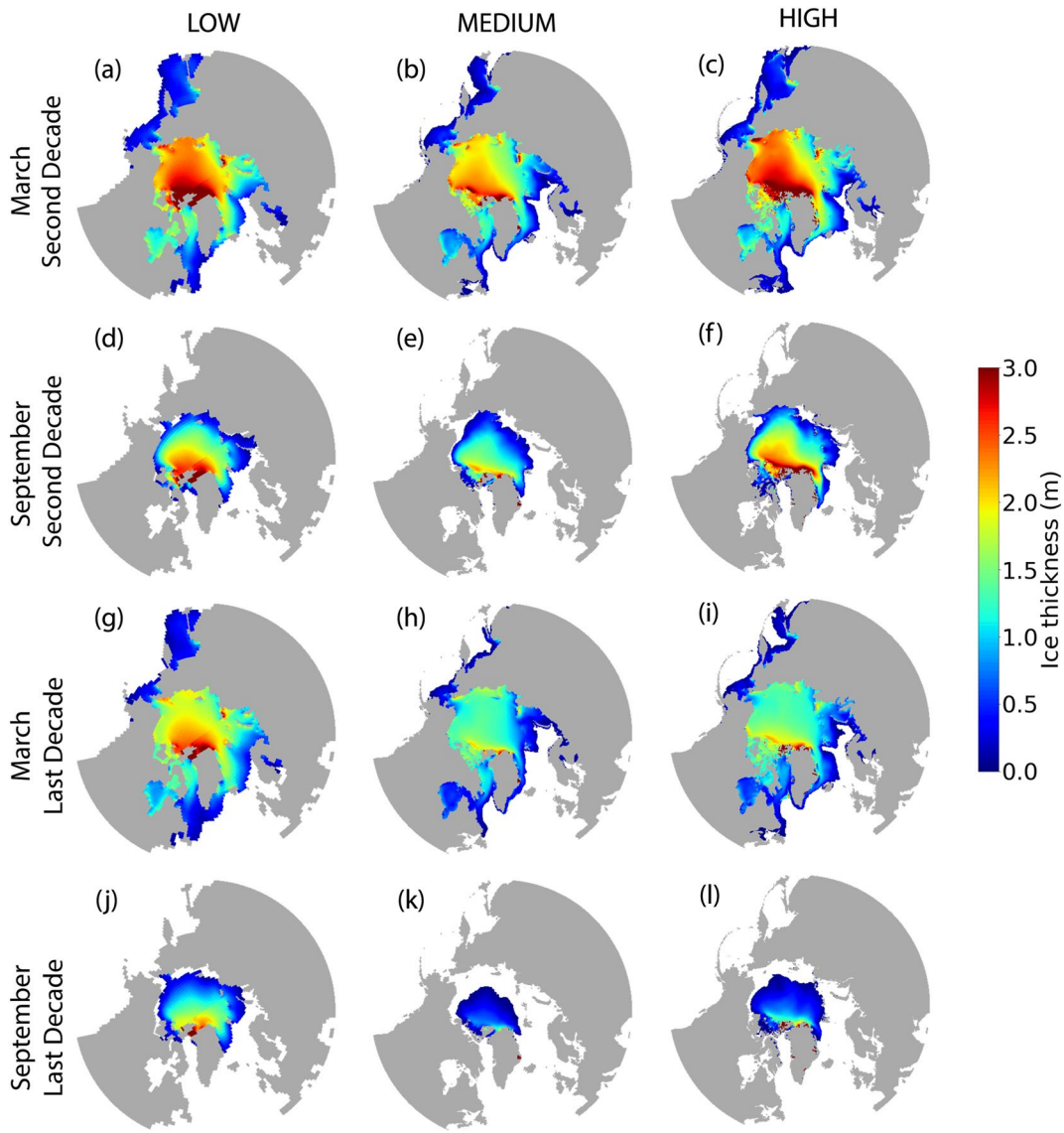

Figure 2. Mean sea ice thickness in the CC simulation averaged over the second decade (a–f) and the last decade (g–l) in March (a–c and g–i) and September (d–f and j–l) for the Low, Medium, and High resolutions. The thicker ice reaches 4.5 m which is within realistic values, and some areas have an accumulation of anomalously thick ice due to the ice being trapped in the simulations (3 km thickness on the coast of Greenland for instance).

from Milly et al. (2014). More details about the suite or individual configurations' performance can be found in Delworth et al. (2012) and Griffies et al. (2015).

In the following sections, we will be discussing the model versions in this order: Medium, High, and Low, as the Medium-resolution model configuration is the closest to the observed SIE and OHT and the Low-resolution model configuration is the farthest.

2.2. Simulations

We analyze a preindustrial control run and a climate change run for each configuration, hereafter referred to as *CTRL* and *CC*, respectively. The CTRL simulation is run for 200 years with constant globally averaged CO_2 concentration of 286 ppmv corresponding to 1860. All model configurations started from the same initial conditions. The CC run branches off from the control run at year 121 with an atmospheric CO_2 concentration increasing at 1% per year over 80 years leading to a doubling of CO_2 levels after 70 years (year 190 of the simulation).

Table 1
Summary of Key Differences Between the Low, Medium, and High-Resolution Model Configurations of the CM2-O Suite

	Low	Medium	High	Observations
Nominal horizontal resolution (°)	1	1/4	1/10	–
Horizontal resolution at 65°N (km)	46 × 111	11 × 11	4 × 4	–
Mesoscale eddy parameterization	Yes	No	No	–
March SIE trend (10^6 km^2/decade)	−0.1	−0.5	−0.5	−0.9
September SIE trend (10^6 km^2/decade)	−0.3	−0.6	−0.6	−1.6
March SIE interannual variability (10^6 km^2)	0.24	0.18	0.23	0.23
September SIE interannual variability (10^6 km^2)	0.41	0.36	0.32	0.44
Fram Strait OHT (TW)	17	37	23	30–42
Bering Strait OHT (TW)	1	5	3	10–20
Barents Sea Opening OHT (TW)	3	76	38	50–70
Davis Strait OHT (TW)	5.1	9.5	18	1–35
Total Arctic OHT (TW)	26.1	127.5	82	91–167
Atlantic OHT at 26.5°N (TW)	670	560	800	1,350

Note. The SIE trends are calculated over the 80 years of the CC simulation, and the observed trends are computed over the equivalent years of CO_2 concentrations (1979–2019; Fetterer et al., 2017). The simulated SIE trends are linear over the 80-year period. Interannual variability is the standard deviation relative to a 5-year running mean. OHT into the Arctic Ocean is defined as positive. The observed OHTs for the Fram Strait, Bering Strait and Barents Sea Opening are from Beszczynska-Möller et al. (2011), and the observational periods are 1997–2009, 1998–2007, and 1997–2007 respectively. The observed OHT for Davis Strait is from Cuny et al. (2004), and the observational period is 1987–1990. The observed Atlantic OHT at 26.5°N is from Johns et al. (2011). The model OHT is the average over the years with equivalent CO_2 concentration to the observation periods.

For the sake of clarity, we refer to the 80 years of the CC run as years 0 to 79 (not 121 to 200) in figures and text. Only one ensemble member was run for each of the configuration of the suite due to the high computational and storage cost of the high-resolution configuration.

In order to compare model output and observations, we use the annual mean CO_2 atmospheric concentration from the Mauna Loa record (Keeling & Keeling, 2017). Note that the actual increase in CO_2 concentration is slower than the 1% CO_2 increase per year of the model. For this reason, the 41 years of satellite era from 1979 to 2020, corresponding to CO_2 concentrations between 336.84 and 414.24 ppm, are compared to 21 years in the CC run (years 16–37). In the following sections, the years between 1930 and 1979, and between years 7 and 16 in the model, are referred to as the "presatellite" period.

2.3. Method

The total Ocean Heat Transport diagnostic (hereafter referred to as OHT) in the CM2-O suite is calculated online at each time step as $\int_{section} \rho_0 c_p U \Theta dS$ where ρ_0 is the constant Boussinesq reference density (=1,035 kg m^{-3}), c_p is the ocean heat capacity (=3992.1 J kg^{-1} K^{-1}), U is the ocean velocity perpendicular to the section, Θ is the potential temperature, and dS is the surface of the grid cell normal to the flow. The OHT at each gate is calculated by integrating the monthly or yearly averaged OHT across the gate and the full water column. Each gate is located on the same constant latitude or longitude grid points in all the configurations, and is defined from the Low resolution for simplicity (Figure 1). We find that the positioning of the gates can have a minor impact on the magnitude of the OHT, but the changes are uniform across the configurations and within the ranges of observation errors at the gates (not shown). Furthermore, the positioning has a negligible impact on the variability (not shown). We analyze monthly mean output from the last 80 years of each simulation, except for the mass and heat transports of the High resolution where we use yearly means due to storage constraints. The interannual variability is defined as the variability around the 5-year running mean.

The Arctic is divided into three sectors in the analysis presented in Section 3.3: the Atlantic sector, the Pacific sector, and the Eurasian sector. The delimitations of those regions are shown in Figure 1.

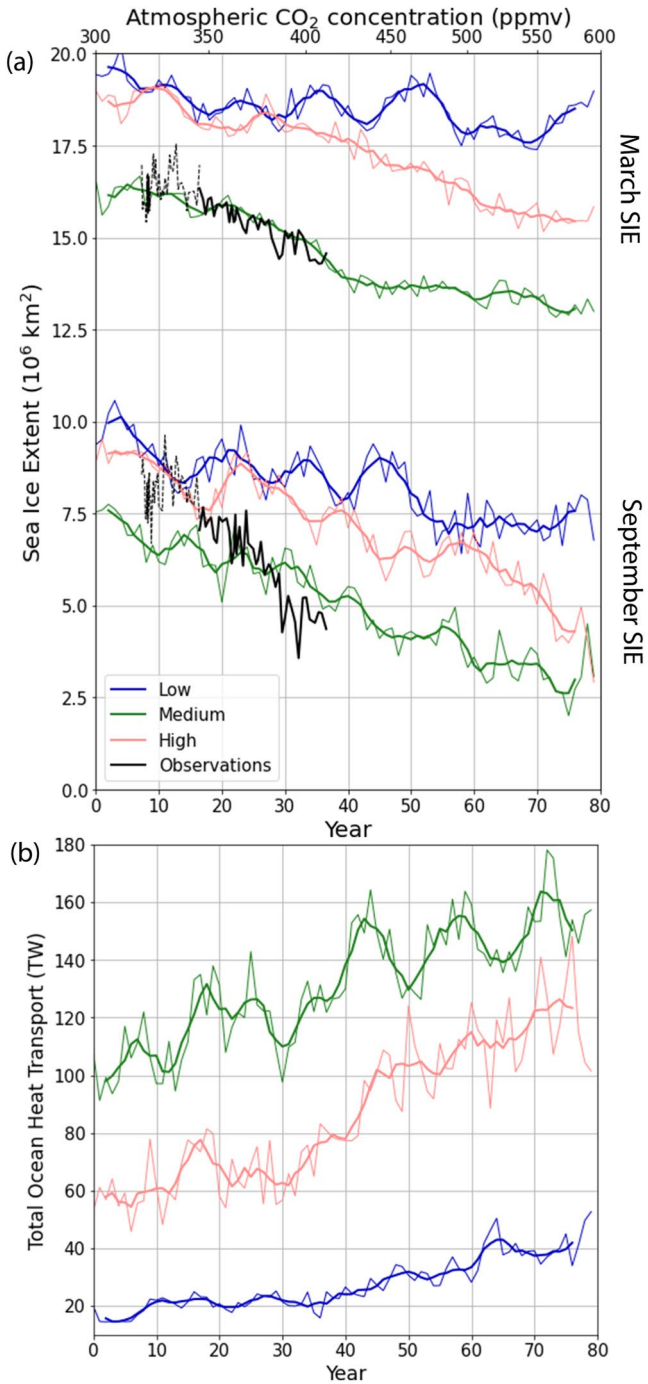

Figure 3. (a) Observed March and September sea ice extent (SIE) between 1930 and 1979 from the presatellite record (dashed black line, Walsh et al., 2019) and between 1979 and 2019 from the satellite record (thick black line, Fetterer et al., 2017), and simulated March and September SIE (thin lines) and 5-year running mean (thick lines) and (b) Yearly mean total OHT into the Arctic as the sum of Barents Sea Opening, Fram Strait and Bering Strait OHT (thin lines) and 5-year running mean (thick lines) as a function of time (model years; bottom axis) and CO_2 concentration (top axis) in the CC run for the Low, Medium, and High resolutions. *Note.* The observations are plotted with respect to the CO_2 concentration for comparison with the model. The SIE is calculated as the area of grid cells where the sea ice concentration exceeds 15%.

3. Results

3.1. Mean Arctic Ocean Climate Over the Presatellite Period

3.1.1. Sea Ice Extent and Thickness

Over the presatellite record, all three configurations reproduce the pan-Arctic winter sea ice thickness distribution with thicker ice on the Canadian side and thinner ice on the Eurasian side of the Arctic, and an east-west asymmetry north of the Canadian Arctic Archipelago (Figures 2a–2c). The winter sea ice thickness in the Low and High resolutions is in general agreement with submarine observations from 1960 to 1982 (Bourke & Garrett, 1987), except along the Alaskan coastline where thicker ice is present in model configurations (2.5–3 m thick ice as opposed to 1–2 m thick ice in observations), indicative of a small bias in the location of the Arctic High. In the Medium resolution, the sea ice is too thin by a few meters in the Central Arctic and Canada Basin (2 m thick ice in the winter as opposed to 3–6 m thick ice in observations), and has a thick bias along the Alaskan coastline that is similar to the other configurations. In the High and Low resolutions, the thicker ice in the East Siberian Sea is typical of climate models, where easterly winds interact with Wrangle Island and the New Siberian Islands (DeWeaver & Bitz, 2006). In the summer, the sea ice thickness is again in general agreement with observations in the Low and High resolutions, and too thin in the Medium resolution (Figures 2d–2f).

In the Medium resolution, the winter and summer SIE are in very good agreement with early satellite observations (Figure 3a). In the winter, in the Low and High resolutions, more sea ice is found in the Bering and Greenland Seas, suggesting a weaker subpolar gyre in both the northern North Pacific and Atlantic (Figures 2a and 2c). The overestimation of sea ice in those regions leads to a larger March SIE in the Low and High resolutions compared to the Medium resolution (Figure 3a). The thick bias in summer SIE is associated with an absence of sea ice melt in all peripheral seas (Figures 2d and 2f). This bias could be due to winter sea ice thickness anomalies in the western Arctic (Figures 2a and 2c), or a smaller summer melt. We will see in Section 3.3 that the sea ice in peripheral seas is strongly correlated with the OHT into the Arctic, which is weaker in the Low and High resolutions. Despite a similar SIE bias, the Low and High resolutions strongly differ in their response to climate change, as the Low resolution has a much weaker trend than the High resolution (see Section 3.2 for details).

The September and March SIE of the Medium resolution are also in very good agreement with observations over the satellite era (1979–2019), with a small underestimation for September SIE, mostly in the Greenland and Barents Seas (Figures 3a and 4). Conversely, in the Low and High resolutions, the September and March SIE (~9 and ~19 million km^2) are too large by about ~1–3 million km^2 in September and 3 million km^2 in March. While the September total SIE is realistic in the Medium resolution, the spatial extent is too extensive in the East Siberian sea and too retreated in the Atlantic sector when compared to the satellite record (Figure 4). In the Low resolution, the September SIE is too large in all three sectors of the Arctic (Figure 4). The High-resolution sea ice is too extensive in the Pacific and Eurasian sectors and in good agreement with the observations in the Atlantic sector (Figure 4). While the Medium resolution simulates the correct SIE, it does so with a much thinner ice cover throughout the simulation (as the initial

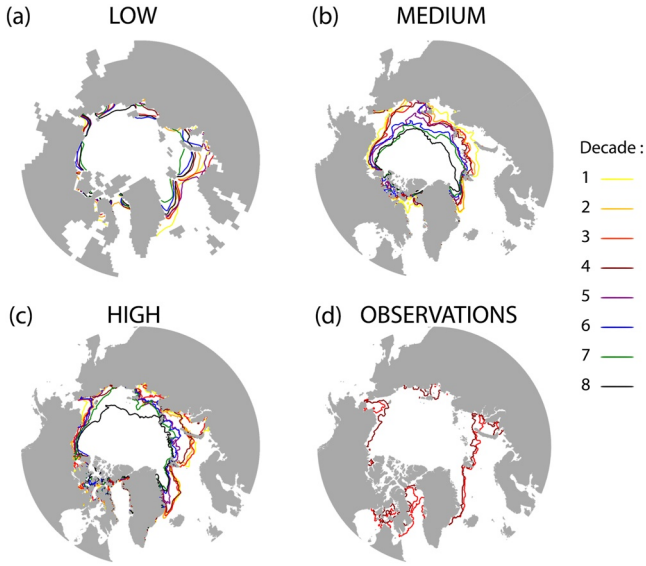

Figure 4. September sea ice edge averaged over each decade of the CC simulation for the (a) Low, (b) Medium, and (c) High resolutions, and for (d) observations over the satellite record. The first decade begins with model year 121 while the last decade ends with model year 200. The satellite era in the model corresponds to the third and fourth decades according to equivalent CO_2 levels.

sea ice thickness is thinner compared to observations from 1960 to 1982, Bourke & Garrett, 1987).

The interannual variability of SIE is in good agreement with observations in all three model configurations (see Table 1), though it is slightly underestimated in September. The increase in interannual variability observed during the transition to a seasonally ice-free Arctic is entirely missing in all the model configurations (not shown, Desmarais & Tremblay, 2021). The decadal variability of SIE is larger than observations in September across the model suite, and in March for the Low resolution (see Figure 3a). Interannual variability and the correlations between SIE and OHT variability is discussed further in Section 3.2.

3.1.2. Ocean Heat Transport

During the observational period (see Table 1, corresponding to the end of the third decade and the beginning of the fourth decade in the model), the Medium resolution has a total OHT of 112 TW into the Arctic and is in good agreement with observations in the Fram Strait. In the Barents Sea Opening, the simulated OHT is slightly overestimated compared to estimates from Beszczynska-Möller et al. (2011), but very close to an observational estimate of 73 TW (Smedsrud et al., 2010). The Low resolution greatly underestimates the total OHT, with little heat entering the Arctic through the Barents Sea Opening and Bering Strait (3 TW and 1 TW respectively; Table 1). The OHT through the Fram Strait is also underestimated, by at least 13 TW. This lack of heat transport is the result of low Atlantic waters intrusion onto the Barents Sea shelf in the Low Resolution compared to the other two configurations (Figures 8a–8c). This is presumably due to discrepancies in the large-scale atmospheric circulation, since OHT variability is mostly driven by volume transport variability (Madonna & Sandø, 2022), rather than its low spatial resolution, given that other climate models with similar spatial resolution simulates much higher ocean heat transport in the Barents Sea Opening (e.g., the Community Earth Sysytem Model, Auclair & Tremblay, 2018). In the High resolution, the OHTs in the Fram Strait and Barents Sea Opening are underestimated by at least 7 TW and 12 TW, respectively (Table 1). All model configurations strongly underestimate the OHT across the Bering Strait with the modeled OHTs reaching at most 50% of the observational estimates. The OHT at 26.5°N in the Low (0.67 PW), Medium (0.56 PW), and High (0.80 PW) resolutions for the third decade are comparable, although somewhat lower, compared to that of the RAPID array (1.35 PW, Johns et al., 2011).

Over the observational period, the Medium resolution is the closest to the observational estimates of total OHT and SIE (Table 1 and Figure 3). Of the three resolutions, that model configuration also carries the most heat into the Arctic (~50% more heat than the High resolution). Both the Low and High resolutions underestimate the OHT and overestimate SIE over the observational period, with the High resolution showing significantly greater OHT but only slightly lower SIE than its lower resolution counterpart. Hence, in the CM2-O model suite, the greater the OHT, the lower the SIE, which suggests a major impact of OHT on SIE, in agreement with several studies (Docquier et al., 2019; Li et al., 2017; Mahlstein & Knutti, 2011; Muilwijk et al., 2019; Sandø et al., 2014).

3.2. Impact of OHT on SIE at a Pan-Arctic Scale

In response to the CO_2 forcing, all configurations show a linear decline in SIE with a clear decadal to multidecadal signal superimposed (Figures 3a and Table 1). The trends in the September SIE in the Medium and High resolutions are around -0.6×10^6 km^2/model decade (significant at the 95% confidence level), much smaller in absolute value than the observed trend of −1.6 million km^2/model decade in the satellite era. We note that, even without adjusting the observed trend to the CO_2 concentration in the model simulation, the trend in observations is still higher than in the model configurations (−0.8 million km^2/decade, Onarheim et al., 2018). The underestimation of September sea ice decline in the CM2-O suite is common among climate models; for instance, the CMIP6 multi-model mean trend is −0.7 million km^2/decade (Shu et al., 2020). The trends in the March SIE are ~50% of the observed trend in the Medium-resolution and High-resolution models (significantly different than zero),

and comparable to that of the 1980–1999 observational record in the Low-resolution model (nonsignificant, not shown). Note that the Medium resolution is in very good agreement with observations over the satellite era.

All three simulations have a weak trend in sea ice extent compared to observations and do not reach an ice-free Arctic (defined as SIE < 1 million km^2; IPCC, 2013) after a doubling of CO_2 concentration. Whether this is caused by too weak OHT in the Arctic or other processes (e.g., atmospheric circulation, cloud phase, etc.) is unclear and beyond the scope of the paper. The minima of SIE reached by the CM2-O suite at the end of the CC simulation are generally higher than in the other models participating in CMIP6. Indeed, the majority of climate model simulations reach a sea ice free Arctic in the summer by the year 2050 with a CO_2 concentration ranging between 500 and 550 ppm depending on the emission scenario (Figure 3 and Table S4 of Notz & SIMIP Community, 2020).

We note that the High resolution loses significantly more sea ice under climate change than the Low resolution (Figures 2 and 3a, and Table 1), though both have very similar initial conditions throughout the preindustrial era (not shown). Conversely, the Medium and High resolutions display the same trends under climate change in both seasons despite starting from very different SIE preindustrial conditions (Figure 3a and Table 1). Hence, the lower SIE at the end of the CC run in the Medium resolution is mostly due to the preindustrial mean state (low initial sea ice cover), rather than to a strong response to the CO_2 increase.

The OHT is sensitive to the CO_2 increase in all three model configurations, but the intensity of the response varies across the configurations (Figure 3b). By the end of the simulation, the total OHT has increased by ∼50% in the Medium resolution while it has doubled in the High and Low resolutions. In the Medium resolution, the OHT increase is mostly linear, with a strong decadal variability. In the Low and High resolutions, a significant multidecadal signal is superimposed on the linear increase in OHT, resulting in two "apparent" stable periods without OHT trends (in the first three decades and last two-three decades) and a relatively rapid increase between the fourth and fifth decades (see Figure 3b).

In the Medium resolution, we see a weak signal at decadal timescale in March SIE in the first half of the record, and a stronger decadal signal in September SIE that persists until the end of the simulation (see Figure 3a). We will see in Section 3.3 that this signal is driven mostly by the OHT from the Atlantic driving sea ice loss in the Greenland and Barents Seas. We note that the signal is not as strong as for the High resolution. Presumably, this is due to the fact that the sea ice cover retreats north of the Barents Sea continental shelf in the middle of the simulation (∼year 30, i.e., between the third and fourth decade; see Figure 4), at which point the ocean heat is not in direct contact with the sea ice anymore (Auclair & Tremblay, 2018). Similarly, at an interannual time scale, the total OHT in the Medium resolution is negatively correlated with the May SIE until ∼year 30, after which the correlation reduces (Figure 5) when the sea ice has completely retreated in the Barents Sea.

In the Low resolution, the decadal variability in SIE and OHT are the largest and smallest (respectively) of the CM2-O suite (Figure 3). Hence, the decadal variability in the pan-Arctic SIE is not dominated by OHT variability in that configuration. We will see in Section 3.3 that the OHT and SIE are linked at regional scale (i.e., in the Atlantic and Pacific sectors), but that the two regional signals are out of phase and not apparent in the total SIE and OHT. At the interannual time scale, the total OHT is significantly correlated with May SIE in the Low resolution from year 23 until year 38, with higher OHT leading to lower SIE. From year 38 onward, no significant correlation is found (Figure 5). Several studies highlight that the atmosphere-ocean coupling is generally weaker and poorly represented when the ocean component is at a low, noneddying spatial resolution (Bryan et al., 2010) resulting in less air-sea fluxes especially in the North Atlantic (Roberts et al., 2016). This weak atmosphere-ocean coupling should in principle lead to stronger correlation between ice edge location and OHT variability, as seen in other low resolution GCMs (e.g., Auclair & Tremblay, 2018). The absence of SIE-OHT coupling in the Low resolution is instead attributed to the very small OHT (nondifferentiable from noise) through the Barents Sea Opening in this configuration.

In the High resolution, the variability in OHT at decadal timescale is linked with variability in September SIE (correlation coefficient of −0.51 significant at the 95% confidence level; Figure 3). At interannual timescale, the total OHT is correlated with September SIE until ∼year 160, and with May SIE in the last 20 years of the simulation, although the signal is not robust (i.e., the correlation is only significant for the last few years; Figure 5). Again, the shift in correlations at year 160 corresponds to a significant retreat of sea ice in the Barents Sea (Figure 4 and discussion in Section 3.3).

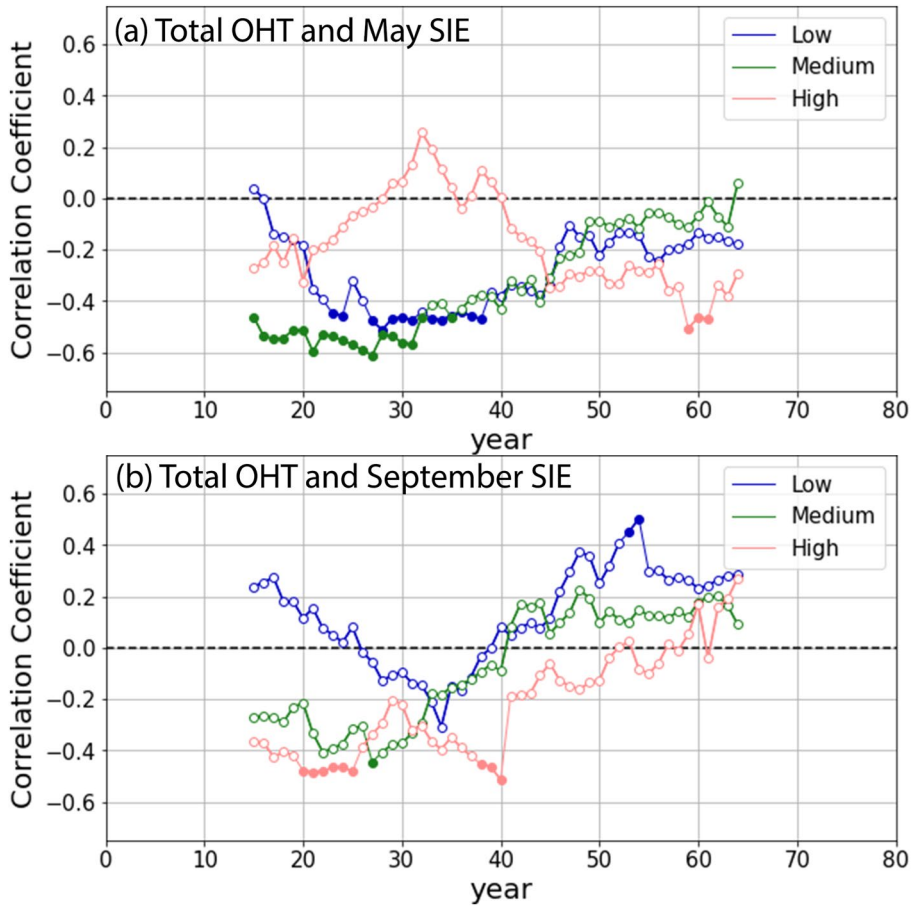

Figure 5. Twenty-year moving window correlation between the detrended annual (January-December) total OHT and the detrended (a) May sea ice extent (SIE) and (b) September SIE in the CC run. Full circles indicate instances where the correlation exceeds the 95% confidence level.

The links between the interannual variability in SIE and total OHT in the CM2-O model suite do not persist throughout the CC simulation, and are not always present in the CTRL simulation (not shown). Hence, OHT variability is not the only driver of SIE variability for any of the model configurations on a global and Pan-Arctic scale, where atmospheric processes also play a key role. However, all configurations show correlations between SIE and OHT at decadal or interannual scale at the beginning of the simulation (except for the September SIE and OHT in the Low-resolution model configuration), which corresponds to the period when sea ice cover is larger, especially in the Barents Sea where a strong influence of the ocean on sea ice is expected (Årthun et al., 2012; Auclair & Tremblay, 2018). This suggests that OHT variability is a major driver of sea ice variability at regional scale, especially when the sea ice extends to the Barents Sea where ocean-ice interactions are more important.

3.3. Impact of OHT on SIE at Regional Scale

3.3.1. Temporal Scales of Correlations Between OHT and SIE

All model versions show an increase in OHT at the three gates concurrent with a decrease in SIE in the three main Arctic sectors in the CC simulations (Figure 6). There is an exception in the March SIE for the Low resolution (Atlantic sector) which shows an increase in SIE (years 165–175) despite the increase in OHT, indicating that the natural variability at decadal timescale in this version is larger than the forced change associated with the CO_2 increase. This partly explains the very weak March SIE trend on the Pan-Arctic scale discussed in Section 3.2. At the multidecadal timescale, the Medium and High resolutions show an abrupt increase in OHT in the Barents Sea Opening at the midsimulation that is concurrent with an abrupt decline in SIE mostly visible in March in the

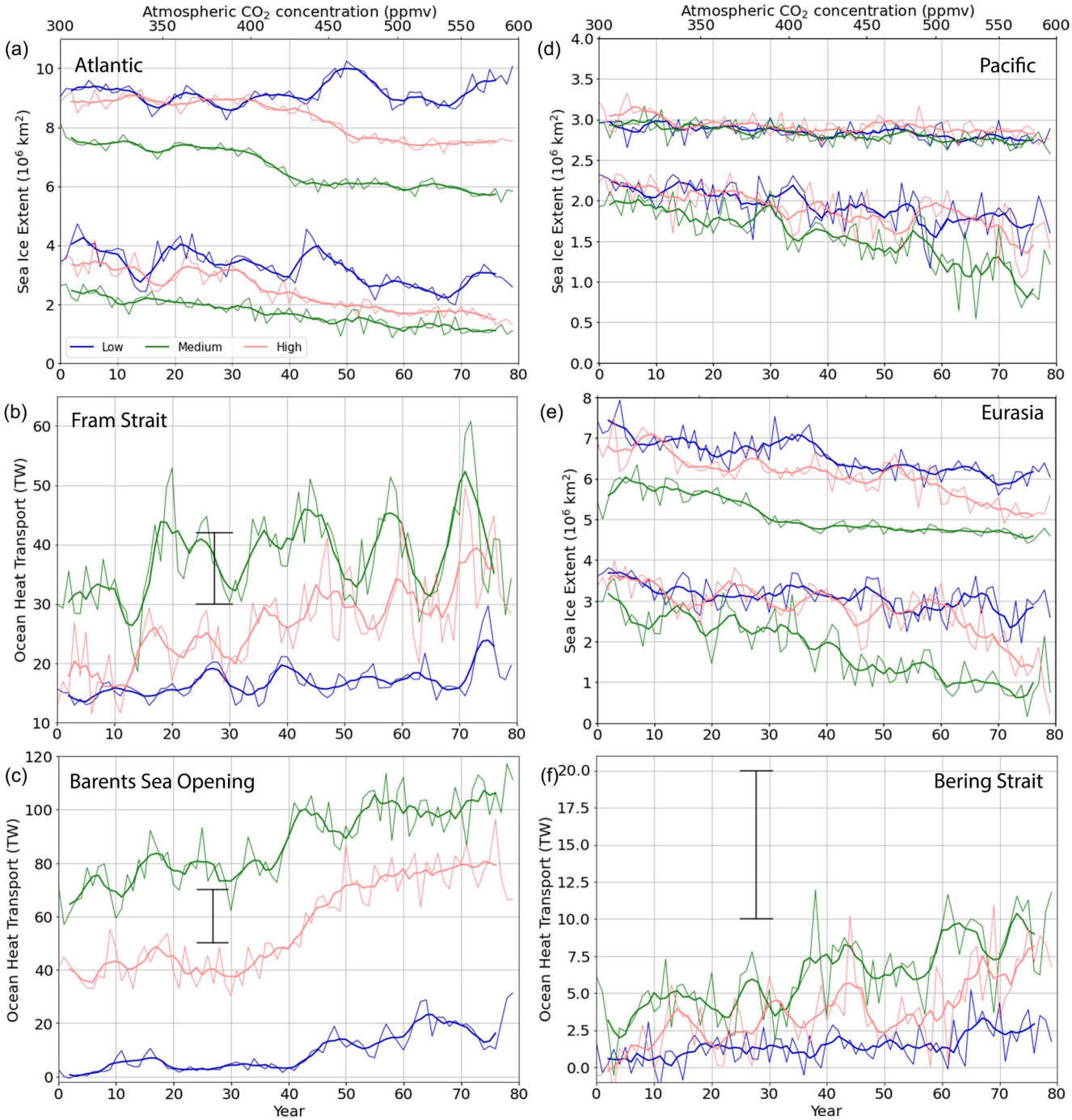

Figure 6. March and September sea ice extent (SIE) (thin lines) and 5 year running mean (thick lines) in (a) the Atlantic sector, (d) the Pacific sector, and (e) the Eurasian sector, and annual Ocean Heat Transport (OHT) (thin lines) and 5 year running mean (thick lines) through (b) the Fram Strait, (c) the Barents Sea Opening, and (f) the Bering Strait in the CC run for the Low, Medium, and High resolutions as a function of time (top axis) and CO_2 concentration (bottom axis). Observational estimates are indicated as vertical bars with the horizontal line corresponding to the time period of observations: (b) 1997–2009 (Schauer & Beszczynska-Möller, 2009), (c) 1997–2007 (Beszczynska-Möller et al., 2011), and (f) 1998–2007 (Woodgate et al., 2010).

Atlantic (Figures 4 and 6a–6c). The September SIE does not react to the abrupt change in Barents Sea Opening OHT, however, as the September sea ice covers only a small part of the Barents Sea shelf. Furthermore, the weak reaction to OHT changes is indicative that summer processes (e.g., ice-albedo feedback) have more impact than later winter preconditioning in the model suite.

In the Medium resolution, the Fram Strait OHT increases in the second decade by about 15 TW, which is concurrent with a very slight local minimum in SIE. The Fram Strait OHT sees another sharp increase of 10 TW in the fourth decade, which is followed by an abrupt increase of 20 TW in the Barents Sea Opening in the fifth decade. Those increases match a sudden decrease in March SIE in the Atlantic sector that is sustained until the end of the simulation (Figures 6a–6c). The Bering Strait OHT increases throughout the simulation, with a sharper increase in the fourth decade that also matches significant sea ice loss in the Eurasian sector (Figures 4b, 6e, and 6f). By the end of the simulation, the OHT in the Bering Strait reaches the lower range of current observations (10 TW).

In the High resolution, the OHT remains fairly constant in the Barents Sea Opening until the fourth decade (equivalent CO_2 concentration around 400 ppmv) when an OHT increase of 30 TW occurs, after which the OHT stabilizes again until the end of the simulation (Figure 6c). These changes match well the pattern of sea ice melt in the Atlantic Sector in March (Figures 4c and 6a). We note that while the September sea ice loss is concurrent with the Barents Sea Opening OHT increase in the High resolution, the March sea ice loss is delayed by ∼10 years. In the Atlantic sector, the decadal variability in the September SIE is driven by Fram Strait and Barents Sea Opening variability in the first half of the simulation (with a significant-correlation coefficients of −0.92 between the September SIE and the Fram Strait and Barents Sea Opening OHT). The decadal variability in the Bering Strait OHT is also well correlated with the decadal variability in September SIE over the whole simulation in the Eurasian Sector (with a significant-correlation coefficients of −0.66 between the September SIE and the Bering Strait OHT), as a sharp increase in Bering Strait OHT in the last 25 years of the simulation is concurrent with a decline in March and September SIE in the Eurasian sector (Figures 6e and 6f).

In the Low resolution, the significant increase in Barents Sea Opening OHT happens around the fourth decade when the OHT goes from near zero to about 20 TW by the end of the simulation. This increase in OHT is concurrent with the retreat of sea ice in the Atlantic sector (Figures 6a and 6c) and especially the Barents Sea (Figure 4a) after the fourth decade. The decadal variability in the Fram Strait and Barents Sea Opening OHT are well correlated with decadal variability in the Atlantic sector September SIE during the first half of the simulation (with a significant-correlation coefficient of −0.69 between the September SIE and the Fram Strait and Barents Sea Opening OHT). In the Eurasian sector, the decrease in SIE at the end of the simulation is concurrent with an OHT increase in the Bering Strait.

3.3.2. Spatial Patterns of Correlations Between OHT and SIE

We now turn to spatial correlations between OHT and Sea Ice Concentration (SIC) anomalies to unravel some major modes of variability at the Pan-Arctic scale and the impact of OHT on sea ice decline at the regional scale.

A tripole between the three sectors defined in Figure 1 appears in the Low and High resolutions, with the Bering Strait OHT and SIC anomalies having opposite sign correlations in the Eurasian sector and the Atlantic/Pacific sector (Figures 7a–7c). In the Medium resolution, the Bering Strait OHT is still positively correlated with the SIC in the Atlantic sector, but negatively correlated in the Pacific sector and on the shelf in the Eurasian sector (we also note an anticorrelation in the Eurasian sector away from the shelf, although it is not significant). This is in accord with results from the CESM-LE (Auclair & Tremblay, 2018), and follows from the fact that, to first order, the volume of water in the Arctic is conserved, hence there is a compensation of ocean volume transport (OVT) between the two sectors (Timmermans & Marshall, 2020). In the Medium and High resolutions, we also find a consistent dipole with opposite sign correlations between SIC variability in the Barents/Greenland seas, and the Labrador Sea. This is a standard signal in the observational record linked with the North Atlantic Oscillation (NAO) variability (Venegas & Mysak, 2000). In the Medium resolution, the correlations are weaker in the Barents Sea Opening because the sea ice edge is retreated northward compared to the Low and High resolutions (see Figures 2 and 4).

In the Medium resolution, the Bering Strait OHT is correlated negatively with most of the Pacific side of the Arctic, even well into the Kara Sea, and is positively correlated with SIC in the Barents Sea and Greenland Sea (Figure 7b). This is in accord with the three major pathways of Pacific Waters into the Arctic: the Alaskan current branch, the branch that spills over the Chukchi shelf and enters the Canada/Makarov Basin, and the branch that stays on the Eurasian shelf (Pickart, 2004; Yamamoto-Kawai et al., 2008). The Fram Strait OHT is strongly linked with sea ice melt in the Greenland Sea, Barents Sea and even in the Chuchki Sea (Figure 7e). The Barents Sea Opening OHT is significantly anticorrelated with SIC in the Central Arctic, and a weak but widespread negative correlation pattern

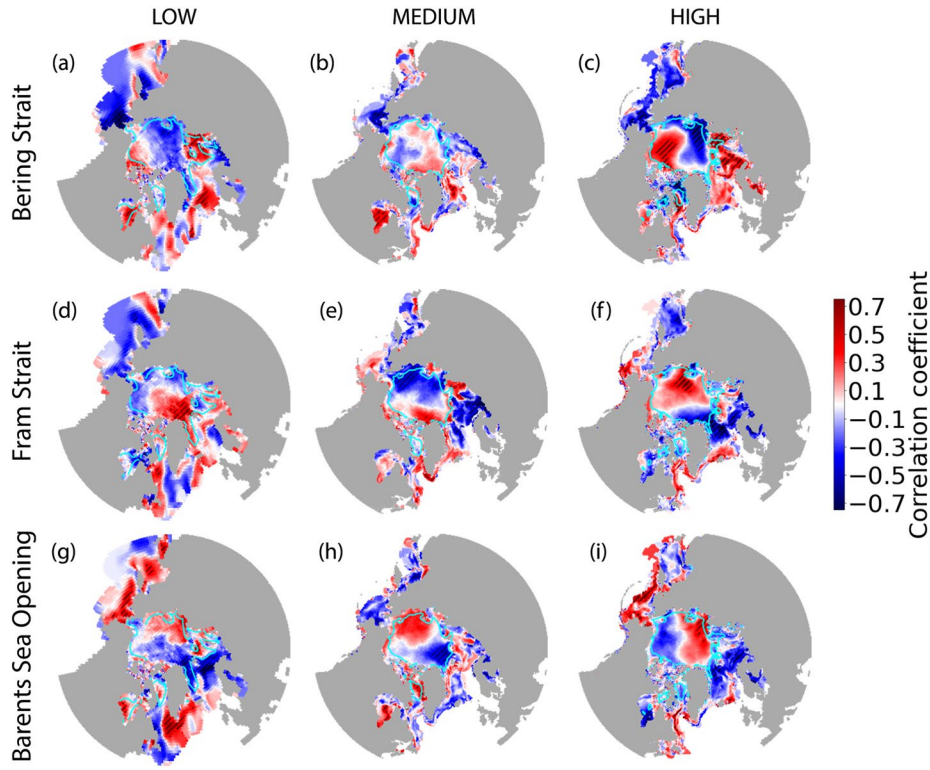

Figure 7. Correlation maps between the detrended annual (January-December) Ocean Heat Transport (OHT) in the Bering Strait (a–c), Fram Strait (d–f) and Barents Sea Opening (g–i) and the detrended May sea ice concentration (SIC), in the Low (left), Medium (center), and High (right) resolutions in the CC experiments. Inside the blue contour lines are areas where the SIC varies by less than 5%. The dashed areas are the 95% significance level. We note that the intensity of the correlation may vary depending on the month used for SIC, but the correlation patterns are similar.

appears in the Barents Sea and in the Eurasian Basin (Figure 7h). The weakness of this negative correlation (nonsignificant at the 95% level) in the Barents Sea is surprising, but could be due to several factors such as the lack of sea ice in that area or the importance of summer processes unrelated to OHT (e.g., surface albedo, etc.). OHTs across the three main gates are shown to be mostly positively correlated with SIC into the Baffin Bay, Hudson Bay, and Labrador Sea, which reflects a partitioning of the heat transport between the Arctic and the Irminger current, associated with the NAO variability Straneo and Heimbach (2013) as we will see in Section 4.

In the Low resolution, we see a significant negative correlation between Bering Strait OHT and SIC in the East Siberian sector (Figure 7a). In this configuration, the branch of Pacific Waters that stays on the Eurasian shelf is dominant for the sea ice variability, in accord with the CESM-LE (Auclair & Tremblay, 2018). The Fram Strait OHT is significantly correlated to sea ice loss in the Greenland Sea and the Labrador Sea, as well as on the Barents Sea Shelf, but positively correlated with SIC around the Fram Strait itself (Figure 7d). Finally, the Barents Sea Opening OHT is strongly correlated with sea ice loss both in the Barents Sea and the Fram Strait (Figure 7g).

In the High resolution, the Bering Strait OHT is negatively correlated with SIC in the Bering Sea and Chuchki Sea, as well as the Baffin Bay. For both Fram Strait and Barents Sea Opening OHT, the negative correlations with SIC are significant in the Greenland Sea, the Fram Strait, and the Barents Sea and Kara Sea (Figures 7f and 7i). We also note that Fram Strait and Barents Sea Opening OHTs are positively correlated with SIC in the Baffin Bay and Labrador sea, although the correlations are less significant (again, this is the typical dipole in SIC in the Barents and Labrador Seas).

This analysis reveals more robust coupling between OHT and SIC at the regional scale, especially in the Atlantic sector where Atlantic sea ice loss is driven by OHT increase, in particular in the Barents Sea as shown in Figure 4. We note that the correlations can weaken depending on the month used for the calculation, as atmos-

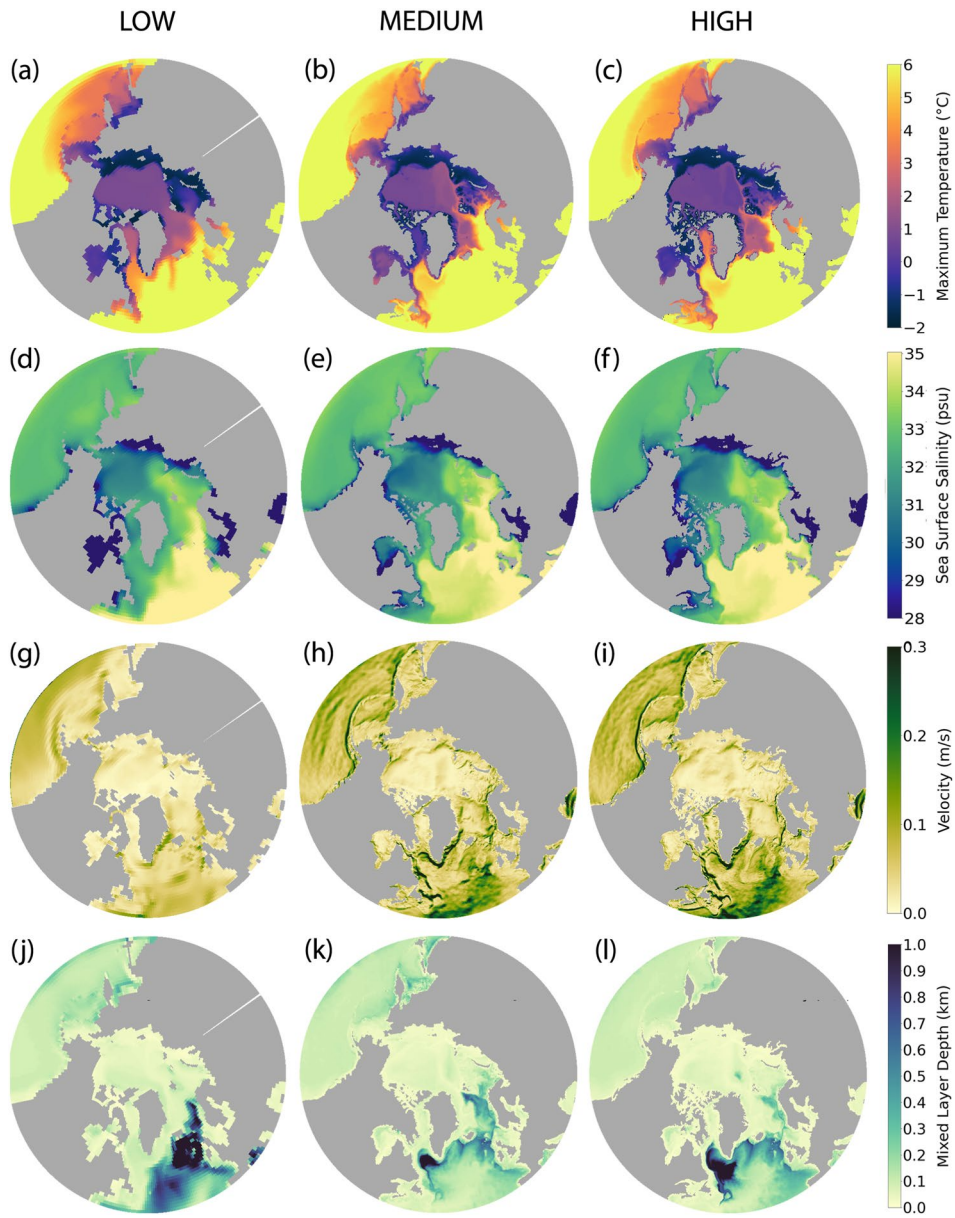

Figure 8. Mean temperature maximum (a–c), sea surface salinity (d–f), surface velocities (g–i), and winter mixed layer depth (h–l) averaged over the first decade (years 120–129) of the CC experiment for the Low (left column), Medium (middle column), and High (right column) resolutions. *Note.* The colorbars are always the same between the configurations.

pheric processes play a more important role in late summer SIE, however the patterns of negative correlations mostly remain consistent (not shown). Significant correlations at interannual and decadal time scales are exhibited between Bering Strait OHT and SIE in the Eurasian Sector, and between the Fram Strait and Barents Sea Opening OHT in the Greenland and Barents Seas.

4. Discussion

Of the three model configurations, the Medium resolution has the largest OHT into the Arctic and smallest winter and summer SIE, both of which are in good agreement with observations. The correct seasonal cycle in SIE is achieved at the expense of a thin bias in sea ice thickness. We find that in the CM2-O suite, the OHT increases with increasing resolution from the Low to the Medium resolution, in agreement with results from Docquier

et al. (2019), but decreases as the resolution increases further from the Medium to the High resolution. This nonmonotonic behavior with spatial resolution is in contrast with other studies, which show a systematic increase in OHT with a finer resolution (Docquier et al., 2019; Grist et al., 2018; Roberts et al., 2016). The possible explanations for this specificity are discussed in this section, with the main candidate being the different partitioning of Atlantic Waters between the Barents Sea Opening, Fram Strait and Irminger Current between the model configurations. Apart from the nonmonotonous increase of OHT with resolution, the other results found in the CM2-O model suite are robust across model families, including weaker ocean heat transport into the Arctic for low resolution (1°) models, and an increase in ocean heat transport northward (North Atlantic Drift or Irminger branch) as the spatial resolution increases (Docquier et al., 2019; Grist et al., 2018; Roberts et al., 2016). This conclusion is robust with respect to the exact location where OHT is calculated: that is, along latitudinal transect at 60°N and 65°N as in Roberts et al. (2016), Grist et al. (2018), and Docquier et al. (2019) or at Arctic gates (results not shown).

The increase in OHT in response to the CO_2 increase is slightly larger in the High resolution than in the Medium resolution, so that the higher OHT and lower SIE in the Medium resolution at the end of the CC simulation are primarily due to the preindustrial mean state. The High-resolution OHT is larger than that of the Low resolution, yet the mean sea ice states in the preindustrial and early CC simulations are similar. This is in contrast with the study by Kirtman et al. (2012) who also find a larger OHT when increasing the resolution in their analysis of the NCAR Community Climate System Model version 3.5 (CCSM3.5) from 1° to 1/10° but a smaller sea ice extent in the High resolution. The low OHT in the NCAR Low-resolution model is mostly attributed to the poor representation of the Norwegian Coastal Current in the model, in accord with results from the CM2-O Low resolution (Figure 8g). The decrease in OHT from the Medium resolution to the High resolution is also in contrast with the results from Hewitt et al. (2016) though the resolution of the atmosphere and the frequency of the ocean/atmosphere coupling is also increased between their two model versions. We note that OHT and SIE correlations are not sensitive to an increase in spatial resolution of the atmosphere component (Docquier et al., 2019). The stronger OHT in the CM2-O Medium resolution occurs despite a weaker AMOC (not shown), in agreement with Oldenburg et al. (2018) and in contrast with results by Jackson et al. (2020). This suggests that the higher OHT in the Medium resolution is linked with the surface ocean circulation (gyre transport) rather than the meridional circulation (Griffies et al., 2015). We argue that differences in current pathways could explain the changes in Arctic OHT in the model versions.

All three model versions agree broadly in the structure of the currents in northern North Atlantic (Figures 8g–8i). The Low resolution however has broader and significantly weaker currents than the Medium and High resolutions over the Arctic. This result is in agreement with Docquier et al. (2019). The most striking difference with the other two resolutions is the absence of the West Greenland Current and Labrador current at the surface (Figure 8g). In the Low resolution, Atlantic Waters enter the Labrador Sea and Baffin Bay at depth (Figures 8a and 8d) and fresh cold Arctic Waters—entering from Lancaster Sound and the Nares Strait - flow southward at the surface. The same top/bottom structure of ocean current is present in the Fram Strait, where Arctic Waters flow southward along the East Greenland coastline and Atlantic Waters flow northward at depth (West Spitsbergen current; results not shown). In the High resolution, Atlantic Waters penetrate far north into the Baffin Bay. The Medium resolution contrasts with the other two resolutions in the Baffin Bay, where very little Atlantic Water enters (Figures 8 and 9b). Instead, Atlantic Waters flow cyclonically around the Labrador Sea along the continental shelf (Figure 8h).

The path of the Atlantic Waters and penetration of heat into the Baffin Bay is known to be influenced by the atmospheric forcing (Holland et al., 2008). In particular, the partitioning of OHT between the North Atlantic Drift and the Irminger Current (south of Iceland) is sensitive to the state of the NAO, with positive phase of the NAO favoring the eastern branch of the circulation, which is then associated with a reduced ice cover in the Greenland and Barents Seas (Myers et al., 2007; Straneo & Heimbach, 2013; Strong et al., 2009). In climate models, the NAO has been shown to influence Labrador Sea Water formation on decadal time scales, which in turn affects the subpolar gyre (Langehaug et al., 2012). During the spin up of our model (years 1–120), the mean state of the atmosphere changes to a more positive NAO state in the Low and High resolutions compared to the Medium resolution (not shown). This state persists throughout the CC simulation (see Figure 10), and should promote deeper penetration of Atlantic Waters in the Fram Strait and Barents Sea Opening in the Low and High resolutions (Langehaug et al., 2012). Instead, we see more recirculation of Atlantic Waters in the Irminger Sea in

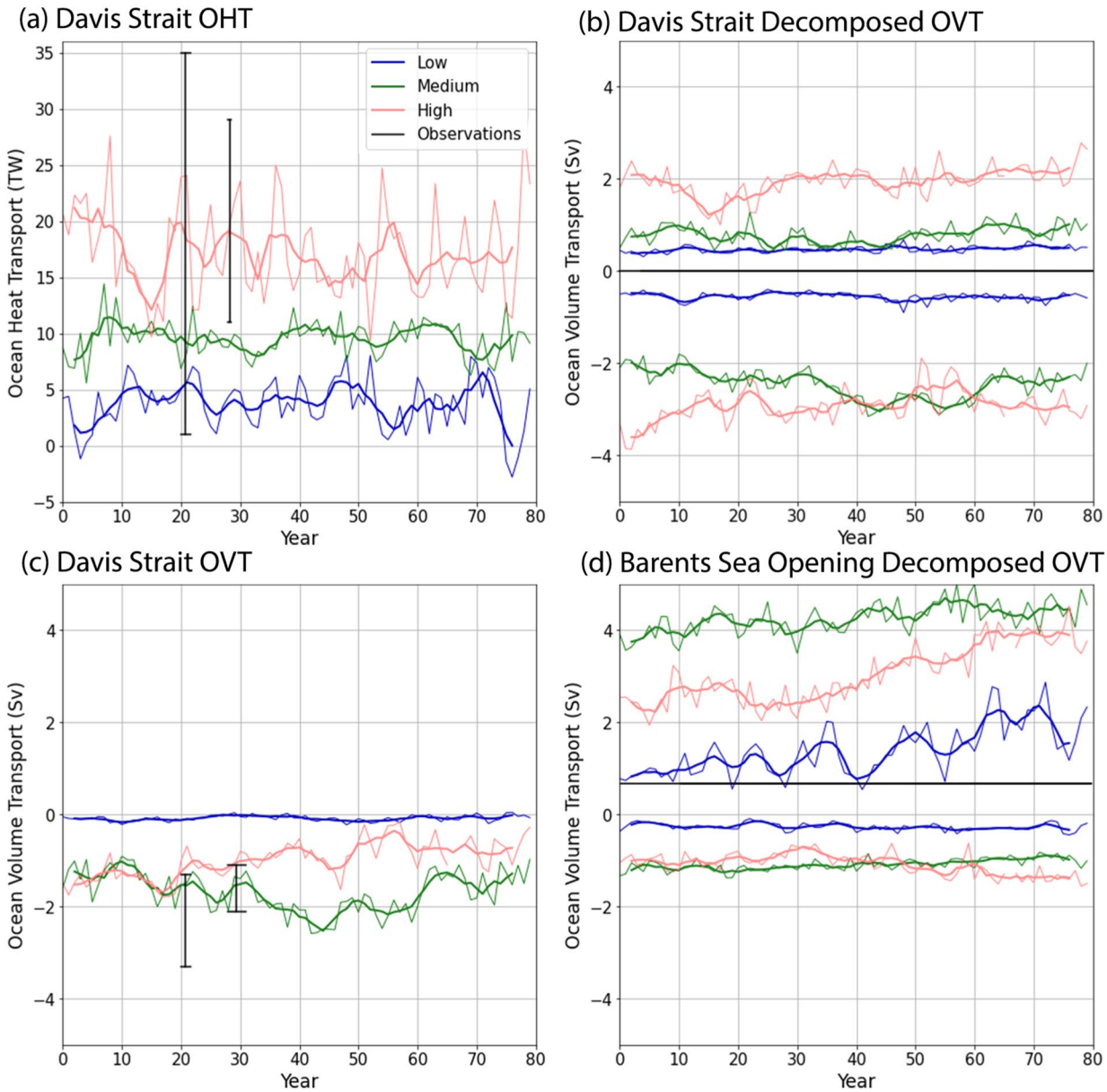

Figure 9. Timeseries of (a) total Ocean Heat Transport (OHT) and (c) total ocean volume transport (OVT) across Davis Strait in the CC run for the Low, Medium, and High resolutions. The total OVT is decomposed into its northward (positive) and southward (negative) component in (b). The same decomposition is made for the Barents Sea Opening OVT in (d). Thin lines correspond to annual averages and thick lines to 5-year running mean. Observational estimates are indicated as vertical bars with the horizontal extent corresponding to the period of observations: 1987–1990 (Cuny et al., 2004) and 2004–2005 (Curry et al., 2011) for OHT, 1987–1990 (Cuny et al., 2004) and 2004–2010 (Curry et al., 2014) for OVT.

the High resolution compared to the Medium resolution, indicating the NAO variability is not the leading factor in determining the current pathways in the Arctic.

The path of warmer Atlantic Waters into the Baffin Bay is also sensitive to spatial resolution in models, with high resolutions (up to 1/60°) favoring the Irminger branch (Pennelly & Myers, 2020). Although all three model configurations fall within the range of observations for OHT through the Davis Strait, the High resolution is the closest to the mean and has the largest interannual and decadal variability of the suite, yet still smaller than observations (Figure 9). Importantly, the OHT across the Davis Strait in the High resolution is the highest across the suite, about twice as large as the OHT in the Medium resolution, and four times that of the Low resolution (Figure 9a). The OVT in the Medium and High resolutions is close to observations, but is much weaker in

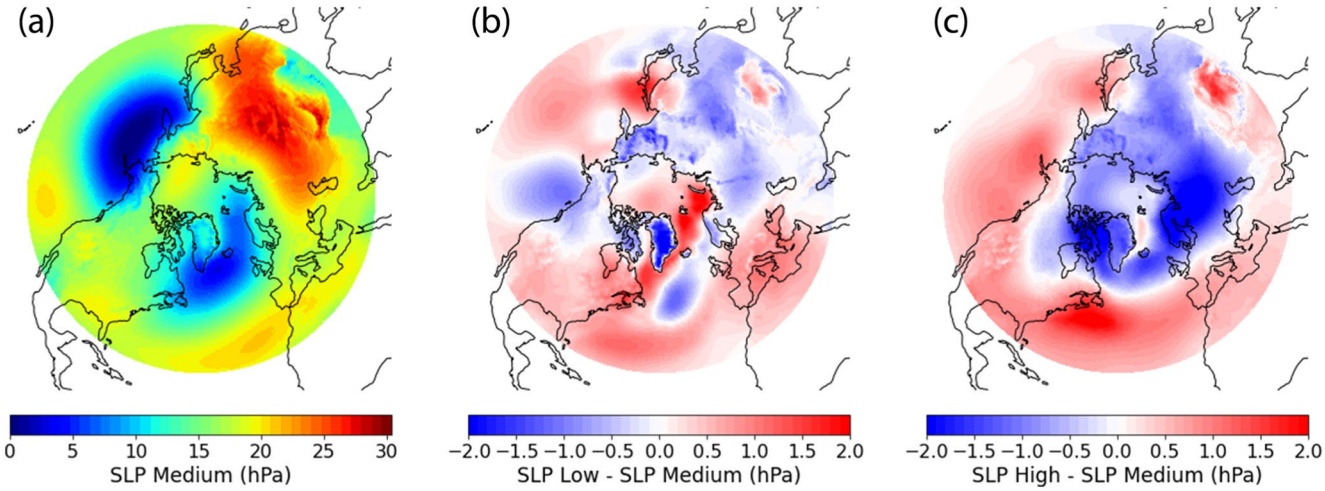

Figure 10. Winter SLP (JFM) in the Medium resolution (a), winter SLP difference between the Low and Medium resolutions (b) and winter SLP difference between the High and Medium resolutions (c) averaged over the CC simulation.

absolute value in the Low resolution (Figure 9c). Very little poleward volume transport is found in the Medium and Low resolutions compared to the High resolution, and the southwards volume transport averages in the Medium and High resolutions are of a similar order (Figure 9b). In the Low-resolution and Medium-resolution configurations, the currents do not penetrate the Baffin Bay and continue along the western boundary toward the Labrador shelf (Figures 8g–8h), whereas in the High-resolution configuration, the current penetrates into the Baffin Bay (Figure 8i). The interannual variability of OVT in Davis Strait is significantly anticorrelated (at the 95% confidence level) with the sum of the transport through the Fram Strait and Barents Sea Opening, with correlation coefficients of −0.82, −0.96, and −0.82 in the Low, Medium, and High resolutions, respectively. This suggests that the Irminger Branch dominates the variability in the Davis Strait as opposed to the East Greenland Current branch bringing polar surface waters southward. This anticorrelation also illustrates the partitioning of the transport of Atlantic Waters between the Arctic and the Labrador Sea and Davis Strait. Hence, in the Medium resolution, the weaker OVT into the Davis Strait is tied to the higher OHT into the Arctic through the Fram Strait and Barents Sea Opening. In particular, the poleward OVT through the Barents Sea Opening is twice as large in the Medium resolution as in the High resolution (see Figure 9d). Furthermore, OHT variability is strongly driven by OVT variability at the interannual and decadal scale, resulting in warmer waters in the Norwegian and Barents Seas. This suggests that the partitioning of OVT into the Arctic is a key component of the representation of the sea ice in the model suite.

In the model suite, the difference in the partitioning of Atlantic waters between the Irminger branch and Norwegian branch can be partly related to the difference in convection centers. In the Medium resolution, mixed layer in the Labrador Sea is slightly deeper but more localized than in the High resolution (Figures 8j–8l). The maximum winter mixed layer depth (MLD) in the Medium resolution is 1.7 km in the first decade of the CC run, around 300 m deeper than in the High resolution. The area of deep convection in the High resolution extends to the western boundary of the Labrador Sea, with MLD of around 1 km. Similarly in the HighResMIP models, 1/4° models show deeper convection than 1° models, and overestimate MLD compared to observations (Koenigk et al., 2021). Pennelly and Myers (2020) also find that increasing the ocean resolution from 1/4° to 1/12° (and even 1/60°) leads to a shallower mixed layer thanks to more representation of eddy fluxes; however, they also find that the area of deep convection is less extensive. Conversely, in the Icelandic and Norwegian Seas, the depth and area of deep mixed layer are greater in the Medium resolution than in the High resolution. From Low to High resolutions, we see a south-westward transfer of deep convection regions from the Greenland-Icelandic-Norwegian (GIN) Seas toward the Labrador Sea (see Figures 8j–8l), in agreement with results from Jackson et al. (2020). These results are also in agreement with those of HadGEM3 and ECMWF, with a shift in convection centers toward the Labrador Sea in 1/4° and 1/12° model configurations, compared to the 1° model (Koenigk et al., 2021, Figure 1).

In the northern North Atlantic, where deep convection is present, we find a strong negative correlation at interannual scale between the OVT across the Barents Sea Opening and winter MLD in both the Medium and High

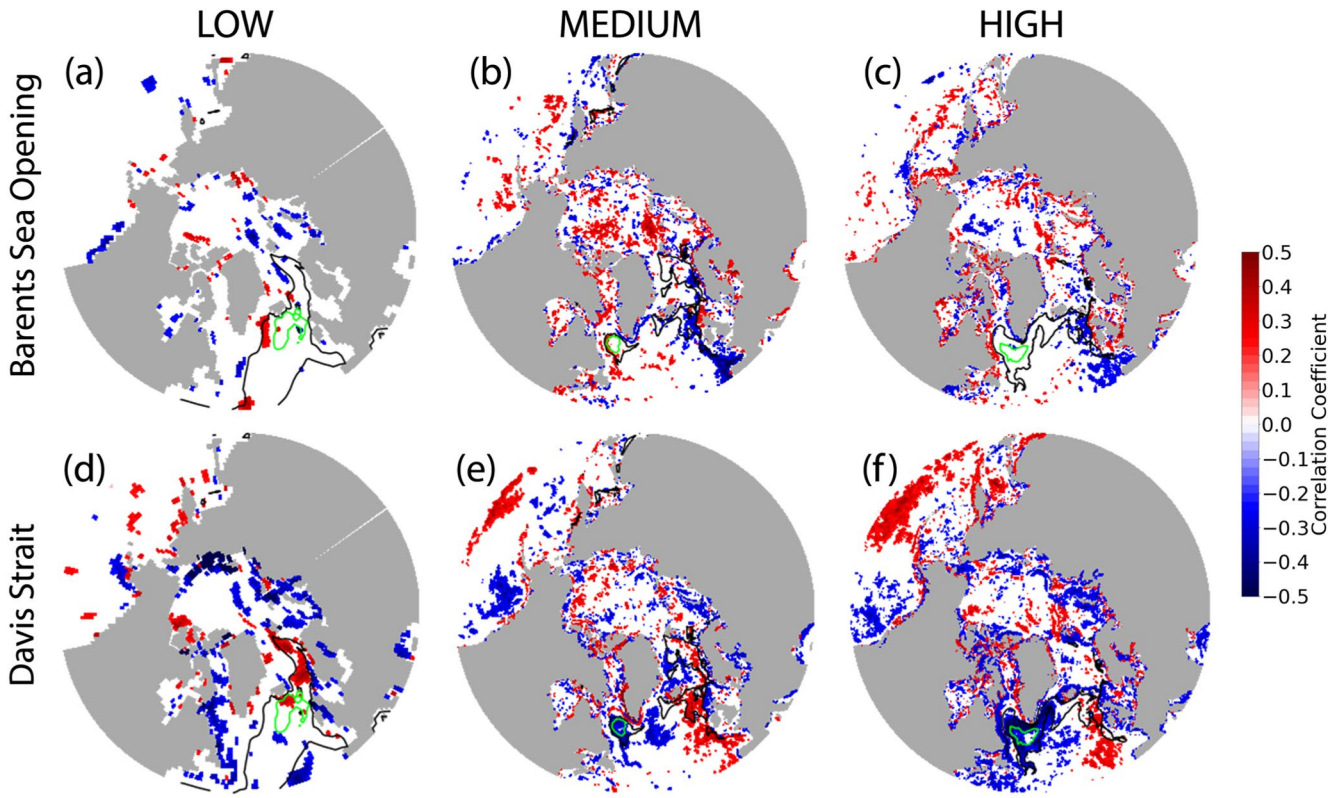

Figure 11. Correlation maps between the detrended annual (January-December) ocean volume transport (OVT) in the Barents Sea Opening (a–c) and Davis Strait (d–f) and the detrended Winter mixed layer depth (MLD), in the Low (left), Medium (center), and High (right) resolutions in the CC experiments. Only correlations that are significant at the 95% level are shown. Black contours indicate the CC simulation average winter MLD at 300 m (black line) and 1 km (green line).

resolutions (Figures 11b, 11c and 8h–8l), indicating that deep penetration of Atlantic Waters into the Barents Sea Opening is associated with weak convection in the GIN Seas. Similarly, the OVT across Davis Strait is negatively correlated with winter MLD in the Labrador Sea in all three model configurations (Figure 11), indicating that deep penetration of Atlantic Waters into Baffin Bay through the Davis Strait is associated with weak convection in the Labrador Sea. This negative correlation suggests that a weak subpolar gyre circulation is associated with strong deep convection and meridional circulation, in agreement with results from Drijfhout and Hazeleger (2006).

5. Conclusion

In this study, we investigated the impact of ocean heat transport on Arctic sea ice under climate change in the GFDL CM2-O model suite. The model suite only differs in the horizontal spatial resolution of the ocean component: from 1° (Low) to 1/4° (Medium) to 1/10° (High), with a mesoscale eddy parameterization for the Low resolution. We investigated the potential impact of resolution on the mean ocean and sea ice states, and the relationship between Arctic ocean heat transport and sea ice, on the Pan-Arctic and regional scale, at annual and decadal timescales. We found that:

1. Models with a higher total ocean heat transport into the Arctic have a smaller sea ice extent in all seasons, in agreement with previous studies (Docquier et al., 2019; Hewitt et al., 2016; Roberts et al., 2016)
2. Decadal variability in ocean heat transport explains a large fraction of decadal variability in sea ice extent
3. At interannual timescale, the impact of ocean heat transport on sea ice extent is limited to the shelf regions
4. The SIE in the Medium-resolution model configuration is in best agreement with the observational record at the beginning of the satellite era
5. In the CM2-O model, the refining of spatial resolution does not induce a systematic increase in OHT, as opposed to other model suites that show a monotonous decrease in sea ice extent with increasing ocean heat transport (Hewitt et al., 2016; Roberts et al., 2016)

6. The shift from noneddying to eddy-permitting resolutions tends to improve the representation of currents and heat transport, particularly in the North Atlantic, in agreement with other studies (Docquier et al., 2019; Roberts et al., 2016)
7. Though the Medium resolution has a higher ocean heat transport and lower sea ice extent when compared with those of the High resolution in the preindustrial mean state, the trends in sea ice loss and ocean heat transport in the two model configurations under increasing CO_2 forcing are similar
8. The Low and High resolutions have the same preindustrial sea ice extent and thickness distribution, but very different response in sea ice extent to CO_2 forcing, with the High resolution being more sensitive than its coarser resolution counterpart
9. As the spatial resolution of the model increases from medium to high, greater heat transport is found into Davis Strait at the expense of the Atlantic-Arctic gates suggesting that the Irminger branch is favored over the Faroe-Scotland branch. The differences in deep convection between these two model configurations might partly explain the difference in heat partitioning

While the increase in OHT and shift of convection centers from east to west of the basin as resolution increases are robust findings across different climate and ocean model families, the lack of sensitivity of sea ice to OHT in Low (eddy-parameterized) is presumably due to the very low OHT in this model. A more complete analysis of different GCMs with eddy-rich ocean component would be required to determine whether the increase in OHT going from eddy-permitting (Medium) to eddy-rich (High) is a robust feature.

In the GFDL CM2-O suite, the poleward heat transport does increase with resolution until about 50°N, with stronger narrower currents. However, the partitioning of the currents in the high latitudes greatly impacts the penetration of heat into the Arctic and in turn the projections of Arctic sea ice. This highlights the need for a realistic representation of said partitioning on top of that of temperature and current strength. The Overturning in the Subpolar North Atlantic Program (OSNAP) provides continuous records of mass and heat transports in the eastern and western subpolar regions against which models' partitioning can be assessed.

Data Availability Statement

All output variables from the the NSIDC are available at https://nsidc.org/data/G02135/versions/3 for monthly sea ice extent and https://nsidc.org/data/G10010 for the SIBT1850 (Sea Ice Back To 1850) data. Output of the GFDL CM2-O suite that were used to make the figures of the paper will be available from the Polar Data Catalog (https://www.polardata.ca/) by acceptance.

Acknowledgments
M. D. acknowledges support from the Fonds de recherche du Québec Nature et technologies (FRQNT) through the Bourse de maîtrise en recherche. M. D. and C. O. D. acknowledge the support of the Natural Sciences and Engineering Research Council of Canada (NSERC)—Accelerator program. M. D. is also grateful for the support of McGill University, Québec-Océan, and Arctrain Canada. This work is a contribution to the NSERC—Discovery Program, Marine Environmental Observation, Prediction and Response (MEOPAR), NASA Grant #80NSSC20K1259, NSF—Office of Polar Program Grants #1504023, #1603350, and #1928126, awarded to BT. We also thank two anonymous reviewers whose constructive comments greatly improved this manuscript.

References

Anderson, J. L., Balaji, V., Broccoli, A. J., Cooke, W. F., Delworth, T. L., Dixon, K. W., & Wyman, B. L. (2004). The new GFDL global atmosphere and land model AM2-LM2: Evaluation with prescribed SST simulations. *Journal of Climate*, *17*(24), 4641–4673.

Årthun, M., Eldevik, T., & Smedsrud, L. H. (2019). The role of Atlantic heat transport in future Arctic winter sea ice loss. *Journal of Climate*, *32*(11), 3327–3341. https://doi.org/10.1175/JCLI-D-18-0750.1

Årthun, M., Eldevik, T., Smedsrud, L. H., Skagseth, Ø., & Ingvaldsen, R. B. (2012). Quantifying the influence of Atlantic heat on Barents sea ice variability and retreat. *Journal of Climate*, *25*(13), 4736–4743. https://doi.org/10.1175/JCLI-D-11-00466.1

Auclair, G., & Tremblay, L. B. (2018). The role of ocean heat transport in rapid sea ice declines in the community earth system model large ensemble. *Journal of Geophysical Research: Oceans*, *123*, 8941–8957. https://doi.org/10.1029/2018JC014525

Barton, B. I., Lenn, Y., & Lique, C. (2018). Observed Atlantification of the Barents sea causes the polar front to limit the expansion of winter sea ice. *Journal of Physical Oceanography*, *48*(8), 1849–1866. https://doi.org/10.1175/JPO-D-18-0003.1

Beszczynska-Möller, A., Woodgate, R., Lee, C., Melling, H., & Karcher, M. (2011). A synthesis of exchanges through the main oceanic gateways to the arctic ocean. *Oceanography*, *24*(3), 82–99. https://doi.org/10.5670/oceanog.2011.59

Bitz, C. M., Fyfe, J., & Flato, G. (2002). Sea ice response to wind forcing from AMIP models. *Journal of Climate*, *15*, 522–536. https://doi.org/10.1175/1520-0442(2002)015<0522:SIRTWF>2.0.CO;2

Bitz, C. M., Holland, M. M., Hunke, E. C., & Moritz, R. E. (2005). Maintenance of the sea-ice edge. *Journal of Climate*, *18*(15), 2903–2921. https://doi.org/10.1175/JCLI3428.1

Bitz, C. M., Holland, M. M., Weaver, A. J., & Eby, M. (2001). Simulating the ice-thickness distribution in a coupled climate model. *Journal of Geophysical Research*, *106*(C2), 2441–2463. https://doi.org/10.1029/1999JC000113

Bitz, C. M., & Lipscomb, W. H. (1999). An energy-conserving thermodynamic model of sea ice. *Journal of Geophysical Research*, *104*(C7), 15669–15677. https://doi.org/10.1029/1999JC900100

Bitz, C. M., & Roe, G. H. (2004). A mechanism for the high rate of sea ice thinning in the Arctic ocean. *Journal of Climate*, *17*(18), 3623–3632. https://doi.org/10.1175/1520-0442(2004)017<3623:AMFTHR>2.0.CO;2

Bourke, R. H., & Garrett, R. P. (1987). Sea ice thickness distribution in the Arctic ocean. *Cold Regions Science and Technology*, *13*(3), 259–280. https://doi.org/10.1016/0165-232X(87)90007-3

Brankart, J.-M. (2013). Impact of uncertainties in the horizontal density gradient upon low resolution global ocean modelling. *Ocean Modelling*, *66*, 64–76. https://doi.org/10.1016/j.ocemod.2013.02.004

Bryan, F. O., Tomas, R., Dennis, J. M., Chelton, D. B., Loeb, N. G., & McClean, J. L. (2010). Frontal scale air-sea interaction in high-resolution coupled climate models. *Journal of Climate*, *23*(23), 6277–6291. https://doi.org/10.1175/2010JCLI3665.1

Cuny, J., Rhines, P., & Kwok, R. (2004). Davis strait volume, freshwater and heat fluxes. *Deep Sea Research Part I: Oceanographic Research Papers*, *52*, 519–542. https://doi.org/10.1016/j.dsr.2004.10.006

Curry, B., Lee, C. M., & Petrie, B. (2011). Volume, freshwater, and heat fluxes through Davis Strait. *Journal of Physical Oceanography*, *41*(3), 429–436. https://doi.org/10.1175/2010JPO4536.1

Curry, B., Lee, C. M., Petrie, B., Moritz, R. E., & Kwok, R. (2014). Multiyear volume, liquid freshwater, and sea ice transports through davis strait. *Journal of Physical Oceanography*, *44*(4), 1244–12661. https://doi.org/10.1175/JPO-D-13-0177.1

Delworth, T. L., Broccoli, A. J., Rosati, A., Stouffer, R. J., Balaji, V., Beesley, J. A., & Zhang, R. (2006). GFDL's CM2 global coupled climate models. Part I: Formulation and simulation characteristics. *Journal of Climate*, *19*(5), 643–674. https://doi.org/10.1175/JCLI3629.1

Delworth, T. L., Rosati, A., Anderson, W., Adcroft, A. J., Balaji, V., Benson, R., & Zhang, R. (2012). Simulated climate and climate change in the GFDL CM2.5 high-resolution coupled climate model. *Journal of Climate*, *25*(8), 2755–2781. https://doi.org/10.1175/JCLI-D-11-00316.1

Desmarais, A., & Tremblay, L. B. (2021). Assessment of decadal variability in sea ice in the community earth system model against a long-term regional observational record: Implications for the predictability of an ice-free Arctic. *Journal of Climate*, *34*(13), 5367–5384. https://doi.org/10.1175/JCLI-D-20-0561.1

DeWeaver, E., & Bitz, C. M. (2006). Atmospheric circulation and its effect on Arctic sea ice in CCSM3 simulations at medium and high resolution. *Journal of Climate*, *19*(11), 2415–2436. https://doi.org/10.1175/JCLI3753.1

Docquier, D., Grist, J. P., Roberts, M. J., Roberts, C. D., Semmler, T., Ponsoni, L., et al. (2019). Impact of model resolution on Arctic sea ice and north Atlantic ocean heat transport. *Climate Dynamics*, *53*(7), 4989–5017. https://doi.org/10.1007/s00382-019-04840-y

Drake, H. F., Morrison, A. K., Griffies, S. M., Sarmiento, J. L., Weijer, W., & Gray, A. R. (2018). Lagrangian timescales of Southern Ocean upwelling in a hierarchy of model resolutions. *Geophysical Research Letters*, *45*, 891–898. https://doi.org/10.1002/2017GL076045

Drijfhout, S. S., & Hazeleger, W. (2006). Changes in MOC and gyre-induced Atlantic ocean heat transport. *Geophysical Research Letters*, *33*, L07707. https://doi.org/10.1029/2006GL025807

Drinkwater, K. F., Miles, M., Medhaug, I., Otterå, O. H., Kristiansen, T., Sundby, S., & Gao, Y. (2014). The Atlantic multidecadal oscillation: Its manifestations and impacts with special emphasis on the Atlantic region north of 60°N. *Journal of Marine Systems*, *133*, 117–130. https://doi.org/10.1016/j.jmarsys.2013.11.001

Dufour, C. O., Morrison, A. K., Griffies, S. M., Frenger, I., Zanowski, H., & Winton, M. (2017). Preconditioning of the Weddell sea polynya by the ocean mesoscale and dense water overflows. *Journal of Climate*, *30*(19), 7719–7737. https://doi.org/10.1175/JCLI-D-16-0586.1

Dunne, J. P., John, J. G., Adcroft, A. J., Griffies, S. M., Hallberg, R. W., Shevliakova, E., & Zadeh, N. (2012). GFDL's ESM2 global coupled climate-carbon earth system models. Part I: Physical formulation and baseline simulation characteristics. *Journal of Climate*, *25*(19), 6646–6665. https://doi.org/10.1175/JCLI-D-11-00560.1

Ferrari, R., Griffies, S. M., Nurser, A. J. G., & Vallis, G. K. (2010). A boundary-value problem for the parameterized mesoscale eddy transport. *Ocean Modelling*, *32*(3), 143–156. https://doi.org/10.1016/j.ocemod.2010.01.004

Fetterer, F., Knowles, K., Meier, W. N., Savoie, M., & Windnagel, A. K. (2017). *Sea Ice index, Version 3*. Boulder, CO: NSIDC, National snow and Ice Data Center. https://doi.org/10.7265/N5K072F8

Flato, G. M. (2011). Earth system models: An overview. *WIREs Climate Change*, *2*(6), 783–800. https://doi.org/10.1002/wcc.148

Fox-Kemper, B., Danabasoglu, G., Ferrari, R., Griffies, S. M., Hallberg, R. W., Holland, M. M., et al. (2011). Parameterization of mixed layer eddies. iii: Implementation and impact in global ocean climate simulations. *Ocean Modelling*, *39*(1), 61–78. https://doi.org/10.1016/j.ocemod.2010.09.002

García-Quintana, Y., Courtois, P., Hu, X., Pennelly, C., Kieke, D., & Myers, P. (2019). Sensitivity of Labrador sea water formation to changes in model resolution, atmospheric forcing, and freshwater input. *Journal of Geophysical Research: Oceans*, *124*, 2126–2152. https://doi.org/10.1029/2018JC014459

Gent, P. R., Willebrand, J., McDougall, T. J., & McWilliams, J. C. (1995). Parameterizing eddy-induced tracer transports in ocean circulation models. *Journal of Physical Oceanography*, *252*(4), 463–474. https://doi.org/10.1175/1520-0485(1995)025_0463:PEITTI_2.0.CO;2

Griffies, S. M., Winton, M., Anderson, W. G., Benson, R., Delworth, T. L., Dufour, C. O., & Zhang, R. (2015). Impacts on ocean heat from transient mesoscale eddies in a hierarchy of climate models. *Journal of Climate*, *28*(3), 952–9771. https://doi.org/10.1175/JCLI-D-14-00353.1

Grist, J. P., Josey, S. A., New, A. L., Roberts, M., Koenigk, T., & Iovino, D. (2018). Increasing atlantic ocean heat transport in the latest generation coupled ocean-atmosphere models: The role of air-sea interaction. *Journal of Geophysical Research: Oceans*, *123*, 8624–8637. https://doi.org/10.1029/2018JC014387

Haarsma, R. J., Roberts, M. J., Vidale, P. L., Senior, C. A., Bellucci, A., Bao, Q., et al. (2016). High resolution model intercomparison project (HighResMIP v1.0) for cmip6. *Geoscientific Model Development*, *9*(11), 4185–4208. https://doi.org/10.5194/gmd-9-4185-2016

Hallberg, R. (2013). Using a resolution function to regulate parameterizations of oceanic mesoscale eddy effects. *Ocean Modelling*, *72*, 92–103. https://doi.org/10.1016/j.ocemod.2013.08.007

Hewitt, H. T., Roberts, M., Mathiot, P., Biastoch, A., Blockley, E., Chassignet, E. P., et al. (2020). Resolving and parameterising the ocean mesoscale in earth system models. *Current Climate Change Reports*, *6*(4), 137–152. https://doi.org/10.1007/s40641-020-00164-w

Hewitt, H. T., Roberts, M. J., Hyder, P., Graham, T., Rae, J., Belcher, S. E., et al. (2016). The impact of resolving the Rossby radius at mid-latitudes in the ocean: Results from a high-resolution version of the met office GC2 coupled model. *Geoscientific Model Development*, *9*(10), 3655–3670. https://doi.org/10.5194/gmd-9-3655-2016

Holland, D., Thomas, R., Deyoung, B., Ribergaard, M., & Lyberth, B. (2008). Acceleration of Jakobshavn Isbr triggered by warm subsurface ocean waters. *Nature Geoscience*, *1*, 659–664. https://doi.org/10.1038/ngeo316

Holland, M. M., Bailey, D. A., Briegleb, B. P., Light, B., & Hunke, E. (2012). Improved sea ice shortwave radiation physics in CCSM4: The impact of melt ponds and aerosols on Arctic sea ice. *Journal of Climate*, *25*(5), 1413–1430. https://doi.org/10.1175/JCLI-D-11-00078.1

Holland, M. M., Bitz, C. M., & Tremblay, B. (2006). Future abrupt reductions in the summer Arctic sea ice. *Geophysical Research Letters*, *33*, L23503. https://doi.org/10.1029/2006GL028024

Hunke, E. C., & Dukowicz, J. K. (1997). An elastic-viscous-plastic model for sea ice dynamics. *Journal of Physical Oceanography*, *272*(9), 1849–1867. https://doi.org/10.1175/1520-0485(1997)027_;1849:AEVPMF_2.0.CO;2

IPCC. (2013). Summary for policymakers. In T. Stocker, D. Qin, G.-K. Plattner, M. Tignor, S. K. Allen, J. Boschung, et al. (Eds.), *Climate change 2013: The physical science basis. contribution of working group I to the fifth assessment report of the intergovernmental panel on climate change* (pp. 1–30). New York: Cambridge University Press. https://doi.org/10.1017/CBO9781107415324.004

Jackson, L. C., Roberts, M. J., Hewitt, H. T., Iovino, D., Koenigk, T., Meccia, V. L., et al. (2020). Impact of ocean resolution and mean state on the rate of AMOC weakening. *Climate Dynamics*, *55*(7), 1711–1732. https://doi.org/10.1007/s00382-020-05345-9

Jahn, A., Kay, J. E., Holland, M. M., & Hall, D. M. (2016). How predictable is the timing of a summer ice-free Arctic? *Geophysical Research Letters*, *43*, 9113–9120. https://doi.org/10.1002/2016GL070067

Jansen, M. F., Adcroft, A. J., Hallberg, R., & Held, I. M. (2015). Parameterization of eddy fluxes based on a mesoscale energy budget. *Ocean Modelling*, *92*, 28–41. https://doi.org/10.1016/j.ocemod.2015.05.007

Johns, W. E., Baringer, M. O., Beal, L. M., Cunningham, S. A., Kanzow, T., Bryden, H. L., & Curry, R. (2011). Continuous, array-based estimates of Atlantic ocean heat transport at 26.5°N. *Journal of Climate*, *24*(10), 2429–2449. https://doi.org/10.1175/2010JCLI3997.1

Keeling, R. F., & Keeling, C. D. (2017). Atmospheric monthly in situ CO_2 data—Mauna loa observatory, Hawaii (archive 2021-09-07). In *Scripps CO_2 program data*. UC San Diego Library Digital Collections. https://doi.org/10.6075/J08W3BHW

Kirtman, B. P., Bitz, C., Bryan, F., Collins, W., Dennis, J., Hearn, N., et al. (2012). Impact of ocean model resolution on CCSM climate simulations. *Climate Dynamics*, *39*(6), 1303–1328. https://doi.org/10.1007/s00382-012-1500-3

Koenigk, T., Fuentes-Franco, R., Meccia, V. L., Gutjahr, O., Jackson, L. C., New, A. L., et al. (2021). Deep mixed ocean volume in the Labrador sea in HighResMIP models. *Climate Dynamics*, *57*, 1895–1918. https://doi.org/10.1007/s00382-021-05785-x

Kurihara, Y., & Tripoli, G. J. (1976). An iterative time integration scheme designed to preserve a low-frequency wave. *Monthly Weather Review*, *1042*(6), 761–764. https://doi.org/10.1175/1520-0493(1976)104<0761:AITISD>2.0.CO;2

Langehaug, H. R., Medhaug, I., Eldevik, T., & Otterå, O. H. (2012). Arctic/atlantic exchanges via the subpolar gyre. *Journal of Climate*, *25*(7), 2421–2439. https://doi.org/10.1175/JCLI-D-11-00085.1

Large, W. G., McWilliams, J. C., & Doney, S. C. (1994). Oceanic vertical mixing: A review and a model with a nonlocal boundary layer parameterization. *Reviews of Geophysics*, *32*(4), 363–403. https://doi.org/10.1029/94RG01872

Li, D., Zhang, R., & Knutson, T. R. (2017). On the discrepancy between observed and CMIP5 multi-model simulated Barents sea winter sea ice decline. *Nature Communications*, *8*(1), 14991. https://doi.org/10.1038/ncomms14991

Madonna, E., & Sandø, A. B. (2022). Understanding differences in north Atlantic poleward ocean heat transport and its variability in global climate models. *Geophysical Research Letters*, *49*, e2021GL096683. https://doi.org/10.1029/2021GL096683

Mahlstein, I., & Knutti, R. (2011). Ocean heat transport as a cause for model uncertainty in projected Arctic warming. *Journal of Climate*, *24*(5), 1451–1460. https://doi.org/10.1175/2010JCLI3713.1

Marzocchi, A., Hirschi, J. J. M., Holliday, N. P., Cunningham, S. A., Blaker, A. T., & Coward, A. C. (2015). The north atlantic subpolar circulation in an eddy-resolving global ocean model. *Journal of Marine Systems*, *142*, 126–143. https://doi.org/10.1016/j.jmarsys.2014.10.007

Mette, M. J., Wanamaker, A. D., Jr, Retelle, M. J., Carroll, M. L., Andersson, C., & Ambrose, W. G., Jr. (2021). Persistent multidecadal variability since the 15th century in the southern Barents sea derived from annually resolved shell-based records. *Journal of Geophysical Research: Oceans*, *126*, e2020JC017074. https://doi.org/10.1029/2020JC017074

Milly, P. C. D., Malyshev, S. L., Shevliakova, E., Dunne, K. A., Findell, K. L., Gleeson, T., & Swenson, S. (2014). An enhanced model of land water and energy for global hydrologic and earth-system studies. *Journal of Hydrometeorology*, *15*(5), 1739–1761. https://doi.org/10.1175/JHM-D-13-0162.1

Molinari, J., & Dudek, M. (1992). Parameterization of convective precipitation in mesoscale numerical models: A critical review. *Monthly Weather Review*, *1202*(2), 326–344. https://doi.org/10.1175/1520-0493(1992)120<0326:POCPIM>2.0.CO;2

Muilwijk, M., Ilicak, M., Cornish, S. B., Danilov, S., Gelderloos, R., Gerdes, R., et al. (2019). Arctic ocean response to Greenland sea wind anomalies in a suite of model simulations. *Journal of Geophysical Research: Oceans*, *124*, 6286–6322. https://doi.org/10.1029/2019JC015101

Murray, R. J. (1996). Explicit generation of orthogonal grids for ocean models. *Journal of Computational Physics*, *126*(2), 251–273. https://doi.org/10.1006/jcph.1996.0136

Myers, P. G., Kulan, N., & Ribergaard, M. H. (2007). Irminger water variability in the west Greenland current. *Geophysical Research Letters*, *34*, L17601. https://doi.org/10.1029/2007GL030419

Notz, D., & SIMIP Community (2020). Arctic sea ice in CMIP6. *Geophysical Research Letters*, *47*, e2019GL086749. https://doi.org/10.1029/2019GL086749

Oldenburg, D., Armour, K. C., Thompson, L., & Bitz, C. M. (2018). Distinct mechanisms of ocean heat transport into the Arctic under internal variability and climate change. *Geophysical Research Letters*, *45*, 7692–7700. https://doi.org/10.1029/2018GL078719

Onarheim, I. H., Eldevik, T., Smedsrud, L. H., & Stroeve, J. C. (2018). Seasonal and regional manifestation of Arctic sea ice loss. *Journal of Climate*, *31*(12), 4917–4932. https://doi.org/10.1175/JCLI-D-17-0427.1

Pacanowski, R., & Gnanadesikan, A. (1998). Transient response in a z-level ocean model that resolves topography with partial cells. *Monthly Weather Review*, *126*(12), 3248–3270. https://doi.org/10.1175/1520-0493(1998)126_3248:TRIAZL_2.0.CO;2

Pennelly, C., & Myers, P. G. (2020). Introducing lab60: A 1/60° nemo 3.6 numerical simulation of the Labrador sea. *Geoscientific Model Development*, *13*(10), 4959–4975. https://doi.org/10.5194/gmd-13-4959-2020

Pickart, R. S. (2004). Shelfbreak circulation in the Alaskan Beaufort sea: Mean structure and variability. *Journal of Geophysical Research: Oceans*, *109*, C04024. https://doi.org/10.1029/2003JC001912

Polyakov, I., Pnyushkov, A., Alkire, M., Ashik, I., Baumann, T., Carmack, E., & Yulin, A. (2017). Greater role for Atlantic inflows on sea-ice loss in the Eurasian basin of the Arctic ocean. *Science*, *356*(6335), 285–291. https://doi.org/10.1126/science.aai8204

Roberts, C. D., Senan, R., Molteni, F., Boussetta, S., Mayer, M., & Keeley, S. P. E. (2018). Climate model configurations of the ECMWF integrated forecasting system (ECMWF-IFS cycle 43r1) for HighResMIP. *Geoscientific Model Development*, *11*(9), 3681–3712. https://doi.org/10.5194/gmd-11-3681-2018

Roberts, M. J., Hewitt, H. T., Hyder, P., Ferreira, D., Josey, S. A., Mizielinski, M., & Shelly, A. (2016). Impact of ocean resolution on coupled air-sea fluxes and large-scale climate. *Geophysical Research Letters*, *43*, 10430–10438. https://doi.org/10.1002/2016GL070559

Saba, V. S., Griffies, S. M., Anderson, W. G., Winton, M., Alexander, M. A., Delworth, T. L., et al. (2016). Enhanced warming of the northwest Atlantic ocean under climate change. *Journal of Geophysical Research: Oceans*, *121*, 118–132. https://doi.org/10.1002/2015JC011346

Sandø, A. B., Gao, Y., & Langehaug, H. R. (2014). Poleward ocean heat transports, sea ice processes, and Arctic sea ice variability in noresm1-m simulations. *Journal of Geophysical Research: Oceans*, *119*, 2095–2108. https://doi.org/10.1002/2013JC009435

Schauer, U., & Beszczynska-Möller, A. (2009). Problems with estimation and interpretation of oceanic heat transport—Conceptual remarks for the case of Fram strait in the Arctic ocean. *Ocean Science*, *5*, 487–494. https://doi.org/10.5194/os-5-487-2009

Semtner, A. J. (1976). A model for the thermodynamic growth of sea ice in numerical investigations of climate. *Journal of Physical Oceanography 62*, 379–389. https://doi.org/10.1175/1520-0485(1976)006_0379:AMFTTG_2.0.CO;2

Shi, X., Notz, D., Liu, J., Yang, H., & Lohmann, G. (2020). Sensitivity of northern hemisphere climate to ice-ocean interface heat flux parameterizations. *Geoscientific Model Development Discussions*, *14*(8),4891–4908. https://doi.org/10.5194/gmd-2020-287

Shu, Q., Wang, Q., Song, Z., Qiao, F., Zhao, J., Chu, M., & Li, X. (2020). Assessment of sea ice extent in CMIP6 with comparison to observations and cmip5. *Geophysical Research Letters*, *47*, e2020GL087965. https://doi.org/10.1029/2020GL087965

Smedsrud, L. H., Ingvaldsen, R., Nilsen, J. E. Ø., & Skagseth, Ø. (2010). Heat in the Barents sea: Transport, storage, and surface fluxes. *Ocean Science*, *6*(1), 219–234. https://doi.org/10.5194/os-6-219-2010

Smith, M., Holland, M., & Light, B. (2021). Arctic sea ice sensitivity to lateral melting representation in a coupled climate model. *The Cryosphere*, *16*, 419–434. https://doi.org/10.5194/tc-2021-67

Straneo, F., & Heimbach, P. (2013). North Atlantic warming and the retreat of Greenland's outlet glaciers. *Nature*, *504*(7478), 36–43. https://doi.org/10.1038/nature12854

Stroeve, J. C., Markus, T., Boisvert, L., Miller, J., & Barrett, A. (2014). Changes in Arctic melt season and implications for sea ice loss. *Geophysical Research Letters*, *41*, 1216–1225. https://doi.org/10.1002/2013GL058951

Strong, C., Magnusdottir, G., & Stern, H. (2009). Observed feedback between winter sea ice and the north Atlantic oscillation. *Journal of Climate*, *22*(22), 6021–6032. https://doi.org/10.1175/2009JCLI3100.1

Timmermans, M.-L., & Marshall, J. (2020). Understanding Arctic ocean circulation: A review of ocean dynamics in a changing climate. *Journal of Geophysical Research: Oceans*, *125*, e2018JC014378. https://doi.org/10.1029/2018JC014378

Tsamados, M., Feltham, D., Petty, A., Schroeder, D., & Flocco, D. (2015). Processes controlling surface, bottom and lateral melt of Arctic sea ice in a state of the art sea ice model. *Philosophical Transactions of the Royal Society A: Mathematical, Physical & Engineering Sciences*, *373*(2052), 20140167. https://doi.org/10.1098/rsta.2014.0167

Ungermann, M., Tremblay, L. B., Martin, T., & Losch, M. (2017). Impact of the ice strength formulation on the performance of a sea ice thickness distribution model in the arctic. *Journal of Geophysical Research: Oceans*, *122*, 2090–2107. https://doi.org/10.1002/2016JC012128

Venegas, S., & Mysak, L. (2000). Is there a dominant timescale of natural climate variability in the Arctic? *Journal of Climate*, *13*, 3412–3434. https://doi.org/10.1175/1520-0442(2000)013⟨3412:ITADTO⟩2.0.CO;2

Walsh, J. E., Chapman, W. L., Fetterer, F., & Stewart, J. S. (2019). *Gridded monthly sea ice extent and concentration, 1850 onward, version 2*. Boulder, CO: NSIDC, National Snow and Ice Data Center. https://doi.org/10.7265/jj4s-tq79

Winton, M. (2000). A reformulated three-layer sea ice model. *Journal of Atmospheric and Oceanic Technology*, *172*(4), 525–531. https://doi.org/10.1175/1520-0426(2000)017⟨0525:ARTLSI⟩2.0.CO;2

Woodgate, R. A., Weingartner, T., & Lindsay, R. (2010). The 2007 Bering strait oceanic heat flux and anomalous Arctic sea-ice retreat. *Geophysical Research Letters*, *37*, L01602. https://doi.org/10.1029/2009GL041621

Yamamoto-Kawai, M., McLaughlin, F. A., Carmack, E. C., Nishino, S., & Shimada, K. (2008). Freshwater budget of the Canada basin, Arctic ocean, from salinity, δ18o, and nutrients. *Journal of Geophysical Research*, *113*, C01007. https://doi.org/10.1029/2006JC003858